5-5-2022

Structural basis of SARM1 activation, substrate recognition, and inhibition by small molecules

Yun Shi

Yo Sasaki

Xianrong Mao

Aaron DiAntonio

Jeffrey Milbrandt

See next page for additional authors

Authors
Yun Shi, Yo Sasaki, Xianrong Mao, Aaron DiAntonio, Jeffrey Milbrandt, and et al.

Article

Molecular Cell

Structural basis of SARM1 activation, substrate recognition, and inhibition by small molecules

Graphical abstract

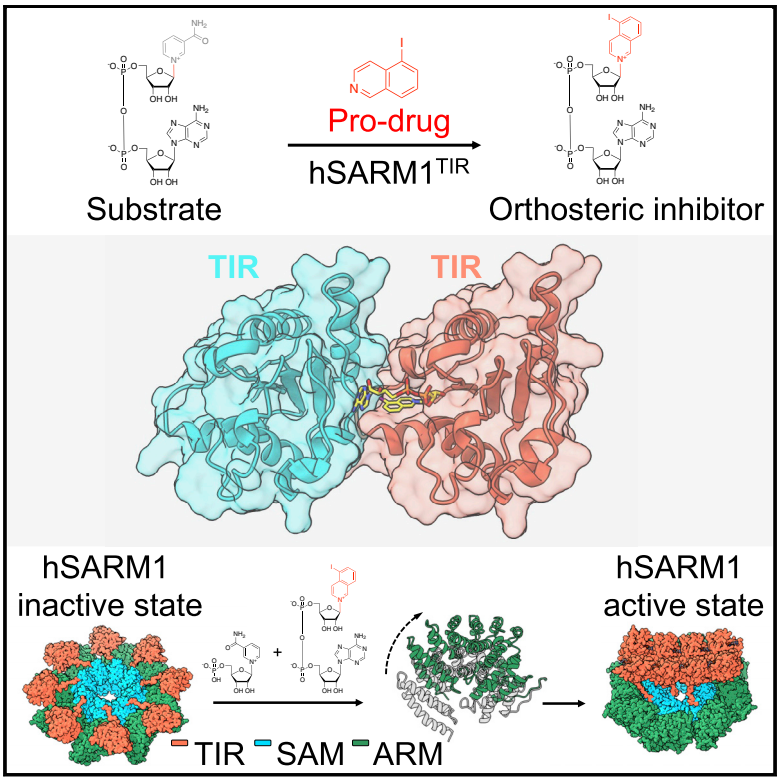

Authors

Yun Shi, Philip S. Kerry, Jeffrey D. Nanson, ..., Jeffrey Milbrandt, Robert O. Hughes, Thomas Ve

Correspondence

rhughes@disarmtx.com (R.O.H.), t.ve@griffith.edu.au (T.V.)

In brief

SARM1 is an inducible pro-neurodegenerative NADase. Shi et al. show that a base-exchange reaction underlies potent orthosteric inhibition of SARM1 by a series of isoquinoline compounds. They also report crystal and cryo-EM structures of SARM1 which reveal the mechanism of substrate binding and how SARM1 is allosterically activated by NMN.

Highlights

- Base exchange underlies potent inhibition of SARM1 at the orthosteric site
- The orthosteric site of SARM1 spans two TIR domain molecules
- Binding of the allosteric activator NMN triggers reorientation of ARM domains
- In the activated state, TIR domains self-associate to form two-stranded assemblies

Shi et al., 2022, Molecular Cell *82*, 1643–1659
May 5, 2022
https://doi.org/10.1016/j.molcel.2022.03.007

CellPress

Molecular Cell

CellPress
OPEN ACCESS

Article

Structural basis of SARM1 activation, substrate recognition, and inhibition by small molecules

Yun Shi,[1] Philip S. Kerry,[2] Jeffrey D. Nanson,[3] Todd Bosanac,[4] Yo Sasaki,[5] Raul Krauss,[4] Forhad K. Saikot,[3] Sarah E. Adams,[2] Tamim Mosaiab,[1] Veronika Masic,[1] Xianrong Mao,[5] Faith Rose,[1] Eduardo Vasquez,[1] Marieke Furrer,[6] Katie Cunnea,[2] Andrew Brearley,[2] Weixi Gu,[3] Zhenyao Luo,[3] Lou Brillault,[7] Michael J. Landsberg,[3] Aaron DiAntonio,[8] Bostjan Kobe,[3] Jeffrey Milbrandt,[5] Robert O. Hughes,[4,*] and Thomas Ve[1,9,*]

[1]Institute for Glycomics, Griffith University, Southport, QLD 4222, Australia
[2]Evotec (UK) Ltd., 114 Innovation Drive, Milton Park, Abingdon, Oxfordshire OX14 4RZ, UK
[3]School of Chemistry and Molecular Biosciences, Institute for Molecular Bioscience and Australian Infectious Diseases Research Centre, University of Queensland, QLD 4072, Australia
[4]Disarm Therapeutics, a wholly-owned subsidiary of Eli Lilly & Co., Cambridge, MA, USA
[5]Needleman Center for Neurometabolism and Axonal Therapeutics and Department of Genetics, Washington University School of Medicine in Saint Louis, St. Louis, MO, USA
[6]Evotec SE, Manfred Eigen Campus, Essener Bogen 7, 22419 Hamburg, Germany
[7]Centre for Microscopy and Microanalysis, The University of Queensland, Brisbane, Australia
[8]Needleman Center for Neurometabolism and Axonal Therapeutics and Department of Developmental Biology, Washington University School of Medicine in Saint Louis, St. Louis, MO, USA
[9]Lead contact
*Correspondence: rhughes@disarmtx.com (R.O.H.), t.ve@griffith.edu.au (T.V.)
https://doi.org/10.1016/j.molcel.2022.03.007

SUMMARY

The NADase SARM1 (sterile alpha and TIR motif containing 1) is a key executioner of axon degeneration and a therapeutic target for several neurodegenerative conditions. We show that a potent SARM1 inhibitor undergoes base exchange with the nicotinamide moiety of nicotinamide adenine dinucleotide (NAD^+) to produce the *bona fide* inhibitor 1AD. We report structures of SARM1 in complex with 1AD, NAD^+ mimetics and the allosteric activator nicotinamide mononucleotide (NMN). NMN binding triggers reorientation of the armadillo repeat (ARM) domains, which disrupts ARM:TIR interactions and leads to formation of a two-stranded TIR domain assembly. The active site spans two molecules in these assemblies, explaining the requirement of TIR domain self-association for NADase activity and axon degeneration. Our results reveal the mechanisms of SARM1 activation and substrate binding, providing rational avenues for the design of new therapeutics targeting SARM1.

INTRODUCTION

Pathological axon degeneration is an early and common hallmark of many neurodegenerative disorders. SARM1 (sterile alpha and Toll/interleukin-1 receptor motif-containing 1), the founding member of a family of Toll/interleukin-1 receptor (TIR)-domain containing enzymes that cleaves the essential metabolite nicotinamide adenine dinucleotide (NAD^+) into nicotinamide (NAM) and adenosine diphosphate ribose (ADPR) (Essuman et al., 2017; Essuman et al., 2018; Horsefield et al., 2019; Wan et al., 2019), is a key executioner of axon degeneration (Coleman and Höke, 2020; Gerdts et al., 2015; Krauss et al., 2020; Sasaki et al., 2020). Loss of SARM1 and its NAD^+ glycohydrolase activity (NADase) protects axons in several neurodegenerative conditions including neuropathies, traumatic brain injury, and glaucoma (Geisler et al., 2016; Gerdts et al., 2013; Henninger et al., 2016; Ko et al., 2020; Marion et al., 2019; Maynard et al., 2020; Osterloh et al., 2012; Turkiew et al., 2017; Ziogas and Koliatsos, 2018).

SARM1 consists of an N-terminal allosteric regulatory armadillo repeat (ARM) domain, two tandem sterile alpha motif (SAM) domains, and a C-terminal catalytic TIR domain (Essuman et al., 2017; Gerdts et al., 2013; Horsefield et al., 2019). Several structures of SARM1 in the inactive state have recently been reported (Bratkowski et al., 2020; Figley et al., 2021; Jiang et al., 2020; Li et al., 2021; Shen et al., 2021; Sporny et al., 2020), showing a central octameric ring of tandem SAM domains (Horsefield et al., 2019; Sporny et al., 2019) with the ARM domains wrapped around the ring and the TIR domains wedged between the ARM domains on the outside of the ring. Self-association of the catalytic TIR domains is required for SARM1 enzymatic function (Horsefield et al., 2019) and their direct interaction with the ARM domains keep them separated from each other.

A rise in the cellular level of the NAD^+ precursor nicotinamide mononucleotide (NMN) promotes SARM1 dependent axon degeneration (Di Stefano et al., 2015; Loreto et al., 2015; Sasaki

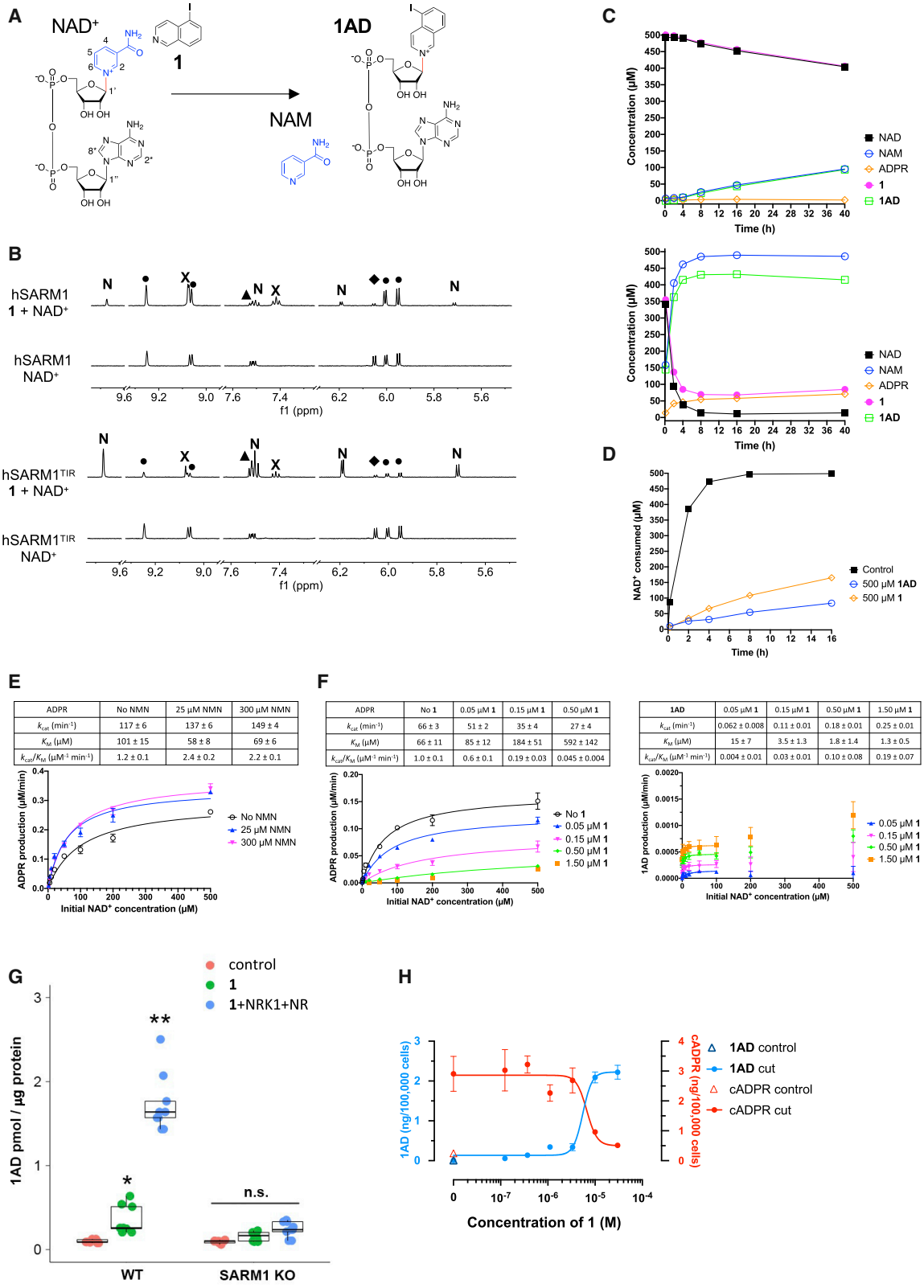

(legend on next page)

et al., 2009), and we have recently shown that SARM1 is activated by an increase in the cellular ratio of NMN to NAD^+ (Figley et al., 2021). Both metabolites compete for binding to the allosteric ARM domain and while both ligand-free and NAD^+-bound SARM1 maintain regulatory ARM:TIR interactions (Bratkowski et al., 2020; Figley et al., 2021; Jiang et al., 2020; Sporny et al., 2020), NMN binding is likely to trigger disruption of these interactions, leading to TIR domain self-association and formation of functional catalytic sites capable of cleaving NAD^+. However, the structural details of this activation process, as well as the requirement of TIR domain self-association for substrate recognition and catalysis, remain poorly understood.

There is great interest in developing SARM1 enzyme inhibitors as candidate therapies for neurodegenerative disorders (Hughes et al., 2021; Krauss et al., 2020; Loring and Thompson, 2020). We have recently reported a potent and selective isoquinoline-derived small-molecule inhibitor (DSRM-3716) of SARM1 NADase activity and demonstrated that it provides protection for injured axons (Hughes et al., 2021). In this study, we uncovered the molecular mechanism of SARM1 inhibition by this compound, demonstrating that it undergoes a base-exchange reaction with the nicotinamide moiety of NAD^+, and that the product, **1AD**, is the bona fide inhibitor. We solved crystal structures of the SARM1 TIR domain in complex with **1AD** and mimetics of NAD^+ produced by similar base-exchange reactions, revealing a substrate binding (orthosteric) site spanning two TIR domain molecules. We further used **1AD** as a tool to capture the active state structure of SARM1 and present cryo-EM structures of the complete SARM1 octamer in complex with the allosteric activator NMN and orthosteric inhibitor **1AD**. These structures show that the ARM domain undergoes a significant reorientation upon NMN binding that disrupts the ARM:TIR regulatory interactions and leads to formation of a two-stranded TIR domain assembly with an architecture and orthosteric site almost identical to our crystal structures. Together, our results explain the mechanisms of SARM1 activation and substrate binding and provide a basis for rational drug design in the treatment of axonopathies.

RESULTS

Mechanism of orthosteric inhibition

Our recently discovered SARM1 inhibitor DSRM-3716, **1** (Figure 1A), recapitulates the $Sarm1^{-/-}$ phenotype and protects axons from degeneration induced by axotomy or mitochondrial dysfunction (Hughes et al., 2021). Notably, **1** showed remarkably strong inhibition (IC_{50} = 75 nM) for its small size (11 heavy atoms). It has a ligand efficiency (LE) value (Hopkins et al., 2004) of 0.88 kcal mol^{-1} heavy $atom^{-1}$, significantly higher than LE values commonly observed for compounds of this size (Hopkins et al., 2004; Hopkins et al., 2014). To investigate the mechanism of inhibition, we first performed real-time NMR-based NADase assays (Figley et al., 2021; Horsefield et al., 2019) with purified human SARM1 (hSARM1) lacking the mitochondrial localization sequence (residues 28–724). While the presence of 500 μM **1** led to a decrease in NAD^+ consumption by hSARM1 (Figure S1A), the appearance of new distinctive NMR peaks (Figure 1B) and a concomitant decrease of the concentration of **1** (Figure 1C) indicate the formation of a new species from **1**. NMR resonances of the new species appeared to be shifting downfield in comparison to the resonances of **1** (Figure 1B), suggesting a de-shielding effect due to loss of electron densities around the corresponding protons. The appearance of new resonances within the anomeric region (5.5 to 6.5 ppm) also indicates that the ribose anomeric carbon is covalently attached to a new group. Thus, we hypothesized that **1** replaced the NAM moiety of NAD^+ to form a base-exchange product, **1AD** (Figure 1B), which could be responsible for the de-shielding effect because of the positive charge on its isoquinoline ring (Figure 1B). A similar base-exchange mechanism has been described for the human NADase CD38 (Preugschat et al., 2008), and hSARM1 was recently shown to catalyze the exchange of the NAM moieties of NAD^+ and nicotinamide adenine dinucleotide phosphate (NADP) with nicotinic acid, 3-acetylpyridine, and vacor (Angeletti et al., 2022; Wu et al., 2021; Zhao et al., 2019). To verify our hypothesis, we employed $hSARM1^{TIR}$, which can catalyze formation of the same new compound (Figures 1B and 1C), to produce and purify **1AD**, and

Figure 1. Mechanism of orthosteric inhibition

(A) Proposed reaction replacing NAM with **1**.

(B) Expansions of NMR spectra showing the appearance of new resonances. Top: 16 h spectra of 0.5 μM hSARM1 + NAD^+ and 0.5 μM hSARM1 + **1** + NAD^+. Bottom: 16 h spectra of 10 μM $hSARM1^{TIR}$ + NAD^+ and 10 μM $hSARM1^{TIR}$ 1 + NAD^+. Resonance peaks from NAD^+, ADPR, NAM, **1**, and the new product **1AD** are labeled as "●", "◆", "▲", "X," and "N," respectively. The initial concentration of compounds (**1** and NAD^+) was 500 μM.

(C) Reaction progression curves of 0.5 μM hSARM1 + 500 μM **1** + 500 μM NAD^+ (top) and 10 μM $hSARM1^{TIR}$ + 500 μM **1** + 500 μM NAD^+.

(D) Inhibition of hSARM1 NAD^+ consumption by 500 μM **1AD** and 500 μM **1**. 0.5 μM hSARM1 was activated by 100 min NMN (500 μM) pre-incubation. Initial NAD^+ concentration was 500 μM.

(E) Kinetic analyses based on ADPR production. 2.5 nM hSARM1 was activated by 120 min pre-incubation with varying concentrations of NMN. Reported values are mean ± SEM, n = 3.

(F) Kinetic analyses of hSARM1, showing ADPR and **1AD** production with varying initial concentrations of **1**. 2.5 nM of SARM1 was pre-incubated with 25 μM NMN for 120 min. Reported kinetic property values are mean ± SEM, n = 3. No stable fit can be obtained for ADPR production in the presence of 1.5 μM **1**. When fitting for **1AD** production, data with more than 100 μM NAD^+ were not used due to an atypical biphasic like behavior that may originate from non-uniform formation of multiple active sites within the SARM1 octamer and their different binding to NAD^+/**1AD**.

(G) SARM1-dependent production of **1AD** in DRG neurons. Statistical analysis was performed by two-way ANOVA with Tukey post hoc test. $F(2, 48) = 111.5$, $p < 2 \times 10^{-16}$ among treatments and genotypes (n = 12). *$p < 0.05$ and **$p < 2x10^{-16}$ denotes statistical significances and n.s. denotes no statistical significance compared with the wild-type protein without **1** (control).

(H) Production of **1AD** in axotomized DRG neurons. DRG neurons were treated with **1** at the concentrations indicated. Axonal **1AD** and cADPR were measured 4 h after axotomy. Data represent means ± SEM, n = 3.

See also Figure S1.

confirmed its structure by NMR and MS analyses (Figure S1C and S1D).

1AD showed improved inhibition of hSARM1 NADase activity compared to **1** itself (Figure 1D). An analog of **1** unable to undergo base exchange showed much weaker inhibition than **1** (Figure S1B), confirming the necessity of the base-exchange reactions to achieve strong inhibition. Further, we performed kinetics assays with hSARM1 (Figures 1E and 1F) using MS and determined apparent kinetic parameters (k_{cat}, K_M, and k_{cat}/K_M) for both ADPR and **1AD** productions in the presence of **1**, at concentrations up to 20 times of its reported IC_{50} value (Hughes et al., 2021). In the absence of **1**, we observed K_M values of between 58 to 101 μM for ADPR production depending on NMN concentration, similar to previously reported values for hSARM1 (Angeletti et al., 2022; Jiang et al., 2020). The presence of NMN only leads to small increases in apparent k_{cat}/K_M values, suggesting that a significant proportion of our purified hSARM1 particles is already in an active state under the conditions used (Figure 1E), and we therefore decided to test the effect of **1** with 25 μM NMN. As expected from our NMR analyses, increasing concentrations of **1** led to a significant decrease in the apparent catalytic efficiency (k_{cat}/K_M) of ADPR production from 1.0 μM^{-1} min^{-1} to 0.045 μM^{-1} min^{-1} with 0.5 μM **1**, while the apparent catalytic efficiency of **1AD** production increased from 0.004 μM^{-1} min^{-1} with 0.05 μM **1** to 0.19 μM^{-1} min^{-1} with 1.5 μM **1** (Figure 1F). The apparent k_{cat} values also revealed that the formation of **1AD** is much slower than that of ADPR within the concentration range tested and slower than similar base-exchange reactions catalyzed by CD38 (Preugschat et al., 2008).

The addition of **1** to dorsal root ganglion (DRG) neurons resulted in the formation of **1AD** (Figure 1G). By contrast, **1AD** was not produced in $Sarm1^{-/-}$ neurons, demonstrating that production of **1AD** in neurons is specific to SARM1 (Figure 1G). Furthermore, upon SARM1 activation by the addition of nicotinamide riboside (NR) in the presence of nicotinamide riboside kinase 1 (NRK1) (Figley et al., 2021), **1AD** production was further increased (Figure 1G). We also treated axotomized DRG neurons with **1** and detected dose-dependent production of **1AD** (Figure 1H). This was inversely correlated with the level of cyclic ADPR (cADPR), a biomarker of SARM1 activity in cells (Sasaki et al., 2020), consistent with SARM1 inhibition by **1** in injured axons (Hughes et al., 2021) (Figure 1H). Taken together, these results demonstrated that **1AD** is the *bona fide* inhibitor of hSARM1, and it is generated *in situ* from its pro-drug **1** by SARM1-specific catalysis in neurons.

The orthosteric site spans two TIR domain molecules

To provide structural insights into this base-exchange mechanism, we determined the structure of a $hSARM1^{TIR}$ crystal soaked with equimolar concentrations of **1** and NAD^+, at 1.72 Å resolution (Table 1). Continuous electron density was observed for a compound corresponding to **1AD**, and the structure revealed an unusual orthosteric site in which **1AD** interacts with both chains (defined here as $hSARM1^{TIR\text{-}A}$ and $hSARM1^{TIR\text{-}B}$) of the asymmetric BB-loop mediated interface (Figures 2A and 2B). This interface, which is also found in TIR domain assemblies involved in Toll-like receptor and interleukin-1 receptor signaling (Clabbers et al., 2021; Ve et al., 2017), was previously shown to be important for $hSARM1^{TIR}$ NADase activity (Horsefield et al., 2019). In the complex, the aromatic ring of the 5-iodo-isoquinoline group engages in interactions with F603 (BB-loop), L607 (αB helix), and W638 (αC helix) of $hSARM1^{TIR\text{-}A}$, while the 5-iodo group forms a halogen bond with the N679 carbonyl group of $hSARM1^{TIR\text{-}B}$ as well as halogen-π interactions with $hSARM1^{TIR\text{-}A}$ F603 and the **1AD** adenine group (Figure 2C). The isoquinoline ribose is located in the conserved cleft between the BB loop and the αB and αC helices in $hSARM1^{TIR\text{-}A}$. The binding mode is similar to the previously determined $hSARM1^{TIR}$:ribose and $hSARM1^{TIR}$:glycerol complexes (Figures S1E and S1F), with the C-2 and C-3 hydroxyls forming hydrogen bonds with the key catalytic residue E642 (Horsefield et al., 2019) (Figure 2C). The diphosphate group is involved in hydrogen-bonding interactions with R569 and the backbone amide of R570 in $hSARM1^{TIR\text{-}A}$, while the adenine group stacks against the indole sidechain of W662 in $hSARM1^{TIR\text{-}B}$ and forms backbone interactions with $hSARM1^{TIR\text{-}B}$ L676, F678, and G680. The adenine-linked ribose is not involved in any direct interactions with either of the chains of the asymmetric interface. Binding of **1AD** does not lead to substantial structural rearrangements in $hSARM1^{TIR}$, compared to the glycerol-bound structure (Figure S1F) (Horsefield et al., 2019). Only small movements in F603 and W662 and a flip of the W638 sidechain are observed.

The binding mode of the inhibitor corroborates the structure-activity relationships observed for a series of isoquinoline-derived compounds (Hughes et al., 2021). The iodine group of the isoquinoline is crucial for high potency, consistent with a strong halogen-bond interaction with N679, as reducing the polarizability of the halogen decreases potency whereas its removal leads to over a 100-fold loss in activity (Figure 2D) (Hughes et al., 2021). Modifications at the 1- and 3-positions lead to significant reductions in activity, most likely due to steric clashes with the adenine-linked ribose, which is consistent with the mechanism of action and binding mode of these isoquinolines. While substitutions at the 4-, 6- and 8-position reduced potency either through steric clashes with the TIR domain or the adenine ring, the 7-position does not affect potency as it points to the bulk solvent. Overall, the binding mode observed in the crystal structure is in agreement with structure-activity data, highlighting the base-exchange reaction that produces an orthosteric site inhibitor **1AD** as the underlying mechanism of its inhibition.

Substrate recognition

The $hSARM1^{TIR}$:**1AD** crystal structure also showed that the base-exchange product retains the same β configuration for its isoquinoline-attached anomeric carbon as for the substrate NAD^+. This is consistent with a double-displacement catalytic mechanism commonly observed in many glycosidases (Heightman and Vasella, 1999; Koshland, 1953), in which a covalent intermediate of glycosyl-enzyme complex is formed (Figure 2E). To test this mechanism, we determined the structure of a $hSARM1^{TIR}$ crystal soaked with araF-NAD^+, which clearly shows a glycosyl-enzyme intermediate with a covalent linkage between a carboxylate oxygen of E642 and the anomeric carbon that was attached to NAM prior to catalysis (Figure 2F). This observation indicates that SARM1 catalysis likely occurs via a covalent intermediate of glycosyl-enzyme complex, although we cannot

Table 1. Crystallographic statistics

	hSARM1^{TIR}:1AD	hSARM1^{TIR}:2AD	hSARM1^{TIR}:3AD	hSARM1^{TIR}:araF-ADPR
Data collection				
Space group	P 2_1 2_1 2	P 2_1 2_1 2	P 2_1 2_1 2	P 2_1 2_1 2
Cell dimensions				
a, b, c (Å)	86.40, 116.40, 32.94	86.24, 116.57, 32.91	86.19, 116.78 33.02	85.51, 117.06, 33.04
α, β, γ (°)	90, 90, 90	90, 90, 90	90, 90, 90	90, 90, 90
Resolution (Å)	47.93 - 1.72 (1.75 - 1.72)	48.29 - 1.79 (1.83 - 1.79)	48.34 – 1.74 (1.77 – 1.74)	48.30 – 1.60 (1.63 – 1.60)
Total reflections	242,073 (12,092)	215,166 (12,595)	234,341 (12,189)	297,557 (13,571)
Unique reflections	36,259 (1830)	32,174 (1854)	35,061 (1814)	44,590 (2,147)
Completeness (%)	99.8 (96.5)	99.9 (97.8)	99.8 (96.7)	99.9 (98.7)
Multiplicity	6.7 (6.6)	6.7 (6.8)	6.7 (6.7)	6.7 (6.3)
Wilson plot B factor (Å^2)	15.00	17.89	19.48	22.78
Rmeas (%)	6.7 (33.3)	8.0 (44.6)	6.3 (45.3)	8.4 (227.2)
Rmerge (%)	6.2 (33.7)	7.4 (41.3)	5.8 (41.7)	7.7 (208.7)
Rpim (%)	2.6 (12.8)	3.1 (16.9)	2.4 (17.3)	3.2 (88.7)
<I/σ(I)>	15.5 (4.3)	12.8 (3.1)	14.4 (3.0)	9.9 (0.9)
$CC_{1/2}$	0.999 (0.957)	0.999 (0.944)	0.999 (0.952)	0.999 (0.578)
Refinement				
Resolution (Å)	48.27 - 1.72	43.12 – 1.79	43.10 – 1.74	35.50 – 1.60
Number of reflections used	36,195	32,116	34,995	44,479
Rwork (%)	15.11	16.83	16.57	20.02
Rfree (%)	17.52	19.94	19.70	22.65
Final model				
Number of protein residues	280	280	280	280
Number of water molecules	280	202	163	123
Number of ligand atoms	92	92	92	34
Average B-factor (Å^2)				
Protein	18	20	24	36
Solvent	31	31	34	40
Ligands	1AD: 22	2AD: 31	3AD: 38	araF-ADPR: 51
Rmsds				
Bond lengths (Å)	0.009	0.010	0.009	0.009
Bond angles (°)	1.195	1.074	1.000	1.041
Ramachandran plot (%)				
Favored	97.10	97.46	97.46	97.10
Allowed	2.90	2.54	2.54	2.90
Outliers	0	0	0	0

The statistics were calculated using AIMLESS (Evans, 2006) and MolProbity (Chen et al., 2010). Statistics for the highest-resolution shell are shown in parentheses. $R_{merge} = \sum_{hkl}\sum_j |I_{hkl\,j} - \langle I_{hkl}\rangle| / (\sum_{hkl}\sum_j I_{hkl\,j})$. R_{work} / $R_{free} = \sum_{hkl} |F^{obs}_{hkl} - F^{calc}_{hkl}| / (\sum_{hkl} F^{obs}_{hkl})$; R_{free} was calculated using randomly chosen 5-10% fraction of data that was excluded from refinement.

exclude the possibility of a mechanism involving an oxocarbenium ion (Zechel and Withers, 2000) stabilized by the negatively charged carboxylate moiety of E642. We next tested if the base-exchange reaction observed for **1** extends to other heterocyclic amines and observed that hSARM1 can catalyze similar reactions with multiple pyridine-fused heterocycles and NAM mimetics either as purified protein or in neurons (Figures 3A, 3B, S1G–S1I, and Table S2). In our NMR assays with purified protein, the biochemical stabilities of the exchanged products vary after their formation, with some reaching a steady concentration and others being cleaved after reaching a maximum concentration (Figures 1C, 3B, S1G, and Table S2), correlating with the electron richness of the heterocyclic ring.

In order to understand the recognition of substrates by hSARM1, we selected **2** and **3** for crystallographic studies, as structures of their base-exchange products, **2AD** and **3AD** (Figure 3A), would better mimic that of the natural substrate NAD^+ than **1AD**. Compound **2** is of particular interest because **2AD** is

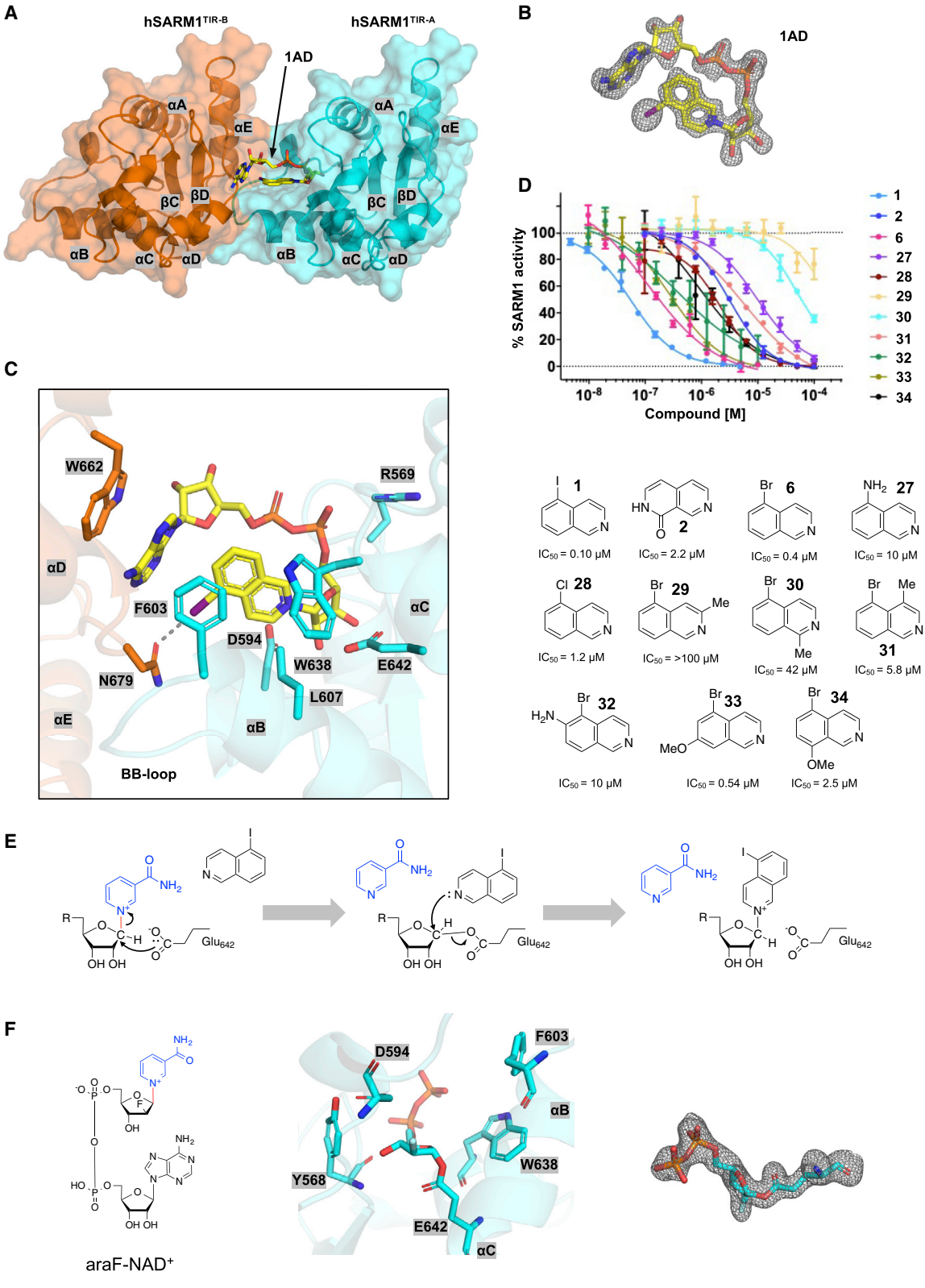

(legend on next page)

the most similar to NAD^+ and is also a substrate of hSARM1 hydrolase activity (Figure S1J). We determined structures of $hSARM1^{TIR}$ crystals soaked with equimolar concentrations of **2** and NAD^+, and **3** and NAD^+, at 1.79 and 1.74 Å resolution, respectively (Table 1). In each structure, continuous electron density was observed for a compound corresponding to the respective base-exchange product (Figure S1K). Similar to **1AD**, both **2AD** and **3AD** interact with both chains of the asymmetric BB-loop mediated interface (Figures 2C and 2D). The adenine group and the diphosphate of these exchanged products form similar interactions with $hSARM1^{TIR}$, but there are significant differences in the binding mode between the exchanged base of **1AD** and that of **2AD** and **3AD** (Figures 3C–3E). Both **2** and **3** lack the halogen group attached to position 5 of the isoquinoline ring of **1**. Instead, **2** has an amide group fused into the bicyclic ring, with its carbonyl oxygen at position 8 engaging with $hSARM1^{TIR}$, whereas **3** has an amine group at position 8 of its isoquinoline scaffold. In comparison to the isoquinoline ring of **1AD**, the 2,7-naphthyridine ring of **2AD** and the isoquinoline ring of **3AD** have flipped 180° with respect to the anomeric linkage and rotated almost 60° anticlockwise about the symmetry axis of the pyridine ring, extending deeper into the active site pocket (Figures 3C–3E) and making less hydrophobic interactions with F603 and W638 than **1AD**. While **2AD** interacts with N679 via its 7-amino group, **3AD** interacts with D594 via its 8-amino group (Figure 3D). The resemblance of **2** and **3** to NAM suggests that NAD^+ is very likely to have a similar binding mode to **2AD** and **3AD**.

Consistent with our structural data, mutations in the binding pocket for nicotinamide ribose and diphosphate groups (Y568A, E642A, R569A, R570A, D594A) have previously been shown to reduce or abolish hSARM1 NADase activity (Essuman et al., 2017; Horsefield et al., 2019). Using mutational analysis, we further verified the importance of residues in the exchanged base and adenine regions of the orthosteric binding site (mutations F603A, W638A, N679A and W662A) on both NADase and base-exchange activities of hSARM1 and $hSARM1^{TIR}$ (Figures 3F and S2). The F603A and W638A mutations would, based on our structures, result in a loss of hydrophobic interactions with the base (NAM, **1**, or **2**). Indeed, both mutants have lower NADase activity and base-exchange activities for **1** and **2** compared to wild-type hSARM1. The N679A mutation, which would be predicted to disrupt halogen bonding with **1AD** and hydrogen bonding interactions with **2AD** and likely NAD^+, has slightly lower NADase activity than wild-type hSARM1 but higher base-exchange activities. The latter is likely a result of reduced inhibition by the base-exchange product, especially **1AD**, upon mutation. The W662A mutation has little effect on the NADase and base-exchange activities of hSARM1. By contrast, W638A, W662A and N679A mutants had much less NADase activity compared to wild-type $hSARM1^{TIR}$ (Figures 3F and S2), indicating that $hSARM1^{TIR}$ is more susceptible to disruptions at the asymmetric dimer interface compared to hSARM1. Taken together, these results support the importance of the identified orthosteric site for the catalytic activities of SARM1.

Cryo-EM structures of activated SARM1

Our crystal structures of $hSARM1^{TIR}$ in complex with **1AD**, **2AD**, and **3AD** suggest that the TIR domains need to dissociate from the ARM domains to oligomerize and form a functional catalytic site, which is supported by mutagenesis studies showing that disruption of the ARM:TIR lock leads to increased hSARM1 activity (Bratkowski et al., 2020; Jiang et al., 2020; Shen et al., 2021). We rationalised that these base-exchange products, which are more biochemically stable than NAD^+ in the presence of SARM1, could be utilized to facilitate the self-association of TIR domains after they dissociate from the ARM domains upon NMN binding, ultimately trapping SARM1 in its active state. We therefore collected cryo-EM data on a hSARM1 sample that had been incubated with NMN and **1AD**. The presence of open-ended curved double-stranded assemblies was apparent from both micrographs and 2D classification (Figures 4A and S3A). Octameric SAM or ARM-SAM domain rings could in some cases be clearly resolved together with the curved double-stranded assemblies while a minor fraction of the particles formed 2D classes that only had intact octameric SAM-ARM domain rings resolved (Figure 4A). The double-stranded assemblies were not observed in a data-set of hSARM1 incubated with NMN alone (Figures S3B and S3E), but we did observe them in a data-set of $hSARM1^{TIR}$ incubated with **1AD**, demonstrating that they consist of TIR domains and that the binding of **1AD** stabilizes these assemblies (Figures S3C and S3F). TIR domain assemblies are also observed in micrographs when incubating hSARM1 with a mixture of NMN and NAD^+ (Figures S3D and S3G); however, the assemblies are shorter and the fraction of particles forming these assemblies is significantly smaller than hSARM1 incubated with NMN and **1AD**.

Single-particle analysis of hSARM1 incubated with NMN and **1AD** yielded reconstructions of the TIR domain assembly with and without octameric rings (SAM-TIR:**1AD**; TIR:**1AD**), and of the octameric ARM-SAM domain ring (ARM-SAM:NMN), at 4.6 Å, 2.9 Å and 3.0 Å overall resolution, respectively (Figures

Figure 2. Structural basis of orthosteric inhibition and catalysis

(A) Structure of the BB-loop mediated $hSARM1^{TIR}$ asymmetric dimer (cartoon and transparent surface; $hSARM1^{TIR-A}$, orange; $hSARM1^{TIR-B}$, cyan) in complex with **1AD** (yellow stick).

(B) Standard omit mFo-DFc map of **1AD**, contoured at 3.0 σ.

(C) Enlarged cutaway of the **1AD** binding pocket in the $hSARM1^{TIR}$ structure.

(D) Inhibition activities of selected isoquinoline-derived compounds. Values represent mean ± SEM; n = 2 (2, 29, 30, 31), 4 (6, 28, 32, 33, 34), 5 (1), and 6 (27).

(E) A simplified model showing a putative catalytic mechanism for hSARM1 base-exchange reactions.

(F) Left, chemical structure of araF-NAD^+; middle, enlarged cutaway view of the partially-resolved catalytic intermediate with araF-ADPR covalently linked to E642 of $hSARM1^{TIR}$; right, standard omit mFo-DFc map of araF-ADPR, contoured at 3.0 σ. Electron density for the leaving NAM group and the adenosine moiety was not observed.

See also Figure S1.

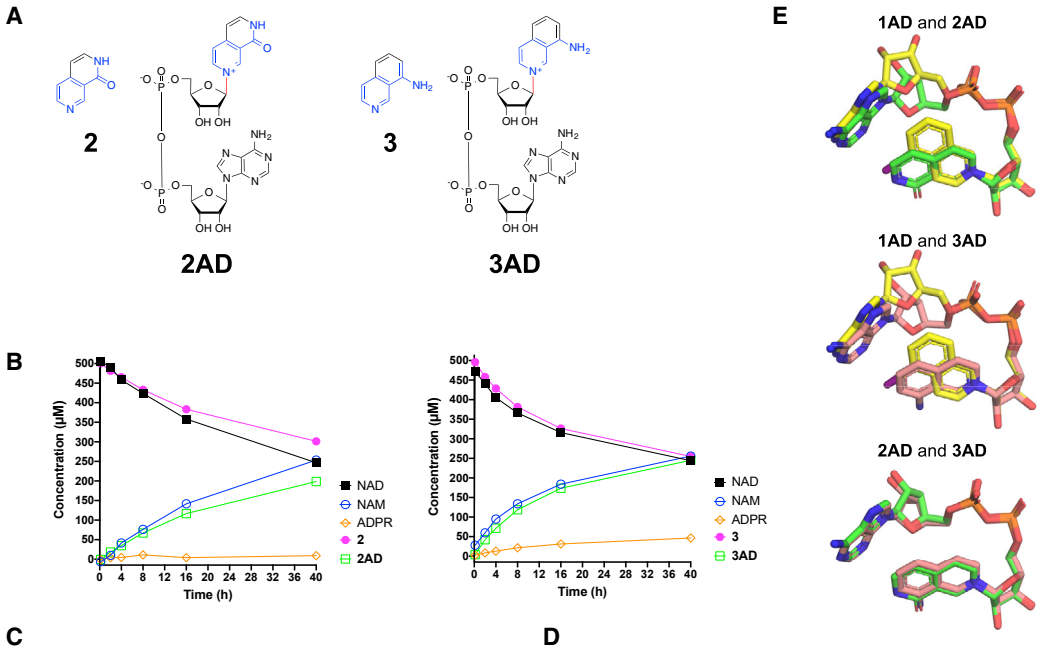

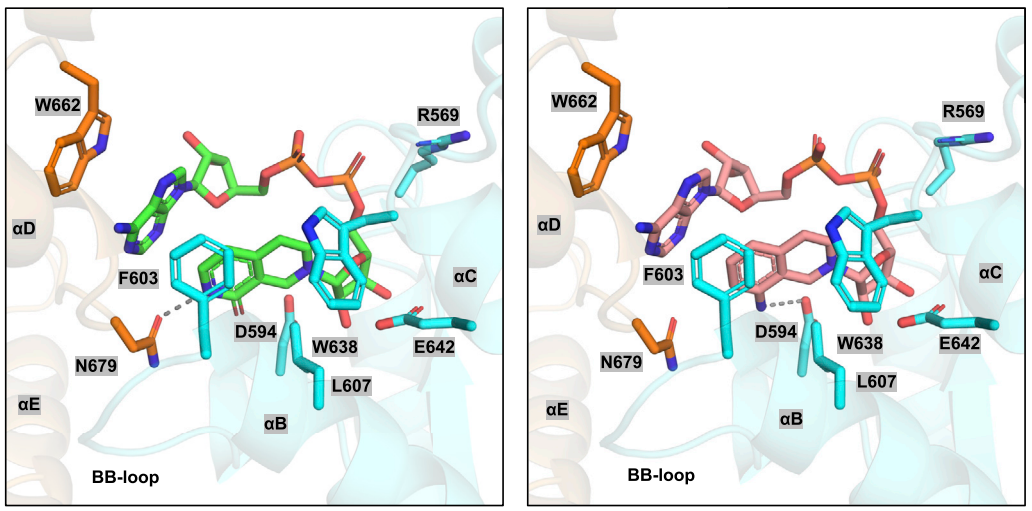

F

Protein	Activity	Time (h)	F603A	W638A	N679A	W662A	H685A	Y687A
hSARM1	NADase	40	43%	64%	64%	108%	7%	4%
	Base-exchange for **1**		55%	59%	212%	94%	27%	7%
	Base-exchange for **2**		24%	24%	124%	80%	15%	8%
hSARM1^{TIR}	NADase	4	0%[#]	22%	21%	15%	6%	5%
	Base-exchange for **1**		2%[#]	99%	105%	103%	76%	2%*
	Base-exchange for **2**		0%[#]	129%	45%	56%	0%	1%

[#]: Protein precipitated under assay conditions
*: Activity increased significantly to normal levels after 16 h

(legend on next page)

S4–S6 and Table S1). The SAM-TIR:**1AD** reconstruction had resolved densities for the SAM and TIR domains only and revealed that the two-stranded TIR domain assembly is located ~15-20 Å above the octameric SAM domain ring (Figures 4B and S4E). The ARM-SAM:NMN reconstruction had well resolved densities for NMN as well as the ARM and SAM domains, but not for the TIR domain, which is probably due to flexibility in the positioning of the ring relative to the TIR domain assembly (Figures 4C, S5, and Table S1). Comparison of this structure to ligand-free and NAD^+-bound hSARM1 structures revealed that the SAM-domain octamers are identical (Figures S7A and S7B), but the ARM domains move upward by 19 Å and undergo a 22° clockwise rotation, with respect to the reported NAD^+-bound and ligand-free structures (Bratkowski et al., 2020; Figley et al., 2021; Jiang et al., 2020; Shen et al., 2021; Sporny et al., 2020) (Figures 4D and S7C). This reorientation leads to a collision between the ARM and TIR domains and puts strain on the SAM-TIR linker (Figures 4E, 4F, and S7D–S7G), resulting in destabilization of the ARM:TIR lock observed in the ligand-free and NAD^+-bound hSARM1 structures (Bratkowski et al., 2020; Figley et al., 2021; Jiang et al., 2020; Shen et al., 2021; Sporny et al., 2020). Analysis of the allosteric site revealed that NMN, which has a similar binding mode as in the $dSARM^{ARM}$:NMN complex, is responsible for this movement of the ARM domain (Figures 4G–4I and S7H–S7K). It pulls on the loop between residues 310–325, causing ARM7 and ARM8 to move toward NMN (Figures 4G and S7J). Because the rigid ARM-SAM linker cannot stretch to accommodate this compaction, it acts as a hinge, causing the ARM domain to lift, rotate (Figures 4D, 4E, and S7C), and clash with the neighboring TIR domain (Figures 4F, S7D–S7G, and Video S1).

The higher resolution TIR domain assembly-only reconstruction had well resolved densities for **1AD** and TIR-domains (Figures 5A and S6G). Although we limited this reconstruction to eight well-defined TIR domain subunits, larger assemblies are visible in both the micrographs (Figure S3A) and 2D classes (Figures 4A and S6A), and they were also detected by analytical size-exclusion chromatography (aSEC) (Figures S3H and S3I), suggesting that **1AD** can induce multiple hSARM1 octameric particles to self-associate via TIR domain interactions under our experimental conditions. However, the lack of larger assemblies for hSARM1 incubated with NMN and NAD^+ in aSEC (Figures S3H and S3I) and the limited number of TIR domain assemblies in the 2D class averages (Figure S3G) suggest that the natural substrate NAD^+, which is rapidly cleaved into NAM and ADPR, is unlikely to induce the formation of these larger assemblies consisting of multiple SARM1 octamers. Citrate was recently reported to induce a phase transition of $hSARM1^{TIR}$ and a ~2,000-fold enhancement in $hSARM1^{TIR}$ NADase activity (Loring et al., 2021). However, we found that the presence of citrate only leads to a minor increase in hSARM1 NADase activity and does not significantly influence its inhibition by **1** (Figure S6H), suggesting that the effect of citrate on TIR domain self-association is not relevant when SAM domains are facilitating TIR domain clustering.

As expected, the hSARM1 double-stranded assemblies consist of two antiparallel strands of TIR domain subunits (Figures 5A–5C and S4F–S4H) and the architecture is identical to the antiparallel two-stranded assembly observed in the $hSARM1^{TIR}$ crystals (Horsefield et al., 2019) (Figure 5D). An active site involving the asymmetric BB-loop mediated self-association interface therefore also forms in the context of full-length hSARM1. Although these assemblies are curved with a ~13° bend per subunit (Figures 5B, 5D, and 5E), both the TIR domain interfaces and the **1AD** binding mode are almost identical to the linear assemblies observed in the $hSARM1^{TIR}$ crystal structure (Figures 5E–5G). The association between the two strands involves the EE loop and αA helices, and in particular the EE loop stabilizes the asymmetric BB loop interface of the adjacent strand, with the highly conserved residues H685 and Y687 interacting with $hSARM1^{TIR\text{-}A}$ and $hSARM1^{TIR\text{-}B}$, respectively (Figure 5C). Alanine mutations of both these residues almost completely eliminate NADase and base-exchange activities for hSARM1 (Figures 3F, 6A, and S2). Both H685A and Y687A mutants also strongly inhibit axon degeneration and have a dominant-negative phenotype (Geisler et al., 2019) (Figure 6B), confirming the essential role of oligomerisation of TIR domains for enzyme activity.

Interestingly, $hSARM1^{TIR}$ displays increased NAD^+ consumption in the presence of bases (Figure S7L) and both the $hSARM1^{TIR}$ H685A and Y687A mutants retained residual NADase activity and normal base-exchange activity for **1**, but not for **2** (Figures 3F and S2). Furthermore, $hSARM1^{TIR}$ orthosteric site mutants W638A, N679A and W662A, all of which have significantly lower NADase activity than the wild-type protein, also showed normal base-exchange activity for **1** but decreased base-exchange activity for **2**, except for the W638A mutant (Figures 3F and S2). As orthosteric ligands bind at the asymmetric BB loop interface, both the substrate and the product may play a role in stabilizing the TIR domain assemblies. It is likely that **1AD**, which has stronger inhibition activity than **2AD** and probably better binding affinity than NAD^+, can better facilitate TIR domain oligomerisation and active site formation of EE-loop and orthosteric site mutants. This was subsequently verified, as **1AD** was shown to activate both $hSARM1^{TIR}$ H685A

Figure 3. Structural basis of substrate recognition

(A) Chemical structures of **2**, **2AD**, **3**, and **3AD**. Parts of the structures are colored blue to indicate resemblance to NAM.

(B) Reaction progression of 0.5 μM hSARM1 + 500 μM **2** + 500 μM NAD^+ (left) and 0.5 μM hSARM1 + 500 μM **3** + 500 μM NAD^+ (right).

(C) Enlarged cutaway view of the **2AD** binding pocket in the $hSARM1^{TIR}$ structure.

(D) Enlarged cutaway view of the **3AD** binding pocket in the $hSARM1^{TIR}$ structure.

(E) Binding modes of **1AD** versus **2AD** (top), **1AD** versus **3AD** (middle), and **2AD** versus **3AD** (bottom).

(F) A summary table of NADase and base-exchange activities of hSARM1 and $hSARM1^{TIR}$ mutants from Figure S2. The activities are shown in percentage relative to the wild-type proteins for 40 h (hSARM1) and 4 h ($hSARM1^{TIR}$) time points.

See also Figures S1 and S2.

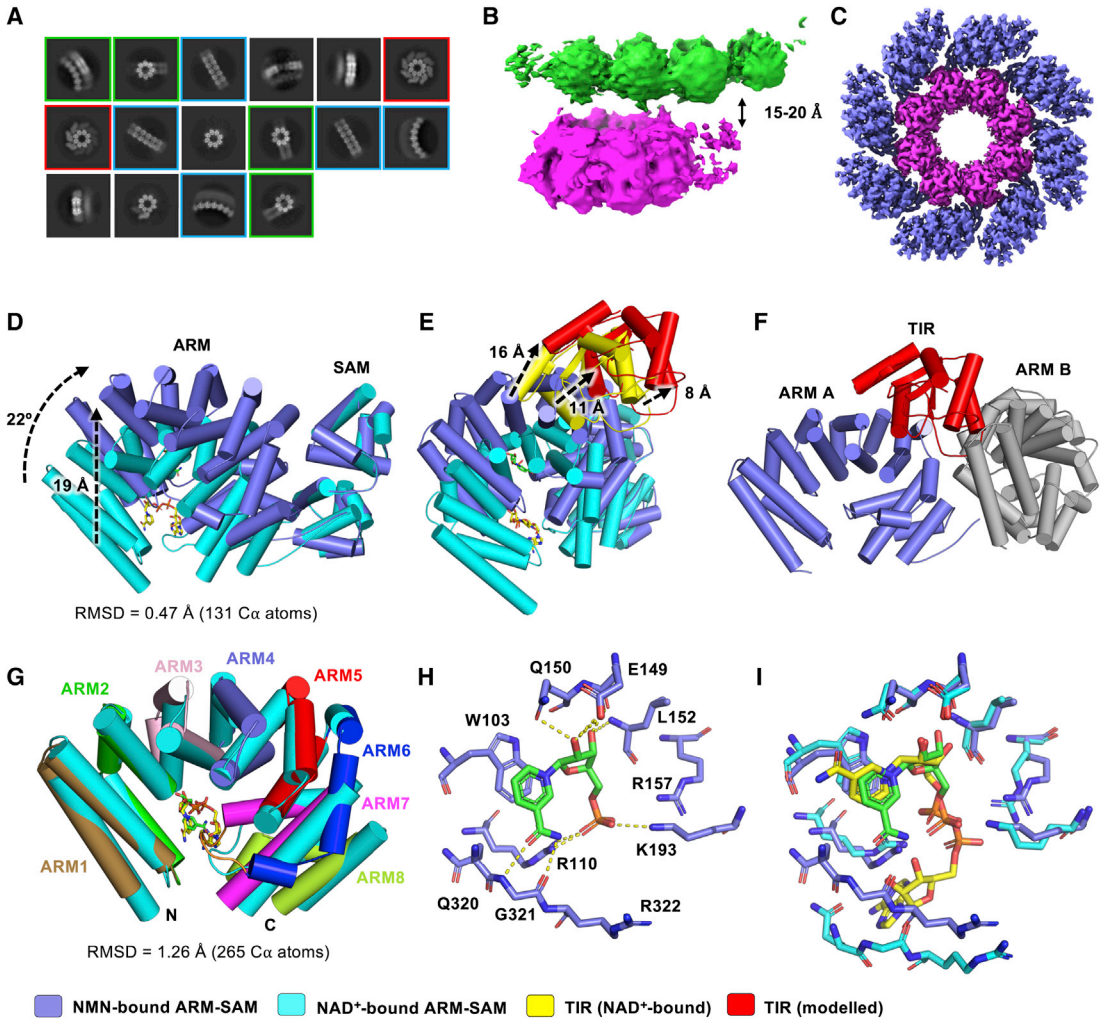

Figure 4. Cryo-EM structures of hSARM1 SAM-TIR:1AD and ARM-SAM:NMN

(A) Representative 2D class averages from hSARM1 incubated with NMN and **1AD**. 2D classes consisting of octameric rings and double-stranded TIR domain assemblies with and without octameric rings are highlighted by red, green, and blue boxes, respectively.

(B) Electrostatic potential density map of SAM-TIR:**1AD**. Map areas corresponding to the TIR and SAM domains are shown in green and magenta, respectively.

(C) Electrostatic potential density map of ARM-SAM:NMN. Map areas corresponding to the ARM and SAM domains are displayed in slate and magenta, respectively.

(D–F) Structural superposition of ARM-SAM:NMN (slate) and hSARM1:NAD^+ (ARM-SAM, cyan; TIR, yellow; PDB: 7ANW). ARM-SAM subunits were aligned by the SAM domain. A hypothetical TIR domain (red) was modeled in ARM-SAM:NMN based on the ARM:TIR interaction observed in hSARM:NAD^+ (PDB: 7ANW). Movement of the ARM and modeled TIR (red) domains induced by NMN binding is indicated by black dashed arrows. NMN and NAD^+ are shown in green and yellow stick representation, respectively. In (D), the superposition shows that the ARM-SAM linker region acts as a hinge to facilitate the translation and rotation of the ARM domain upon NMN binding. In (E), the effect of NMN-induced ARM domain reorientation on the TIR domain (red) is highlighted, while in (F), the resulting clash between the TIR domain and the next ARM domain (gray) in the octameric ring is shown.

(G) Structural superposition of the ARM domains in ARM-SAM:NMN (colored by ARM motif; 310–325 region highlighted in orange) and hSARM1:NAD^+ (cyan; PDB: 7ANW).

(H) Interactions between ARM domain and NMN (stick representation) in ARM-SAM:NMN. Polar contacts are shown as yellow dashed lines.

(I) Comparison of the allosteric sites in ARM-SAM:NMN (slate) and hSARM1:NAD^+ (cyan; PDB: 7ANW). The superposition shows that several of the NMN and NAD^+ interacting residues adopt similar conformations. Notable exceptions are residues 320–322, which move approximately 4 Å, to accommodate NMN; these conformations appear incompatible with NAD^+ binding.

See also Figures S3–S5 and S7.

and Y687A mutants at certain concentrations, while **2AD** only showed inhibition (Figure 6C). Furthermore, **1AD** could slightly activate the hSARM1 H685A mutant at relatively lower concentration (Figure 6D).

Together, these results confirm that in the active state, the TIR domains of hSARM1 form a substrate-stabilized two-stranded open-ended assembly connected to the SAM-ARM octameric ring via flexible linkers.

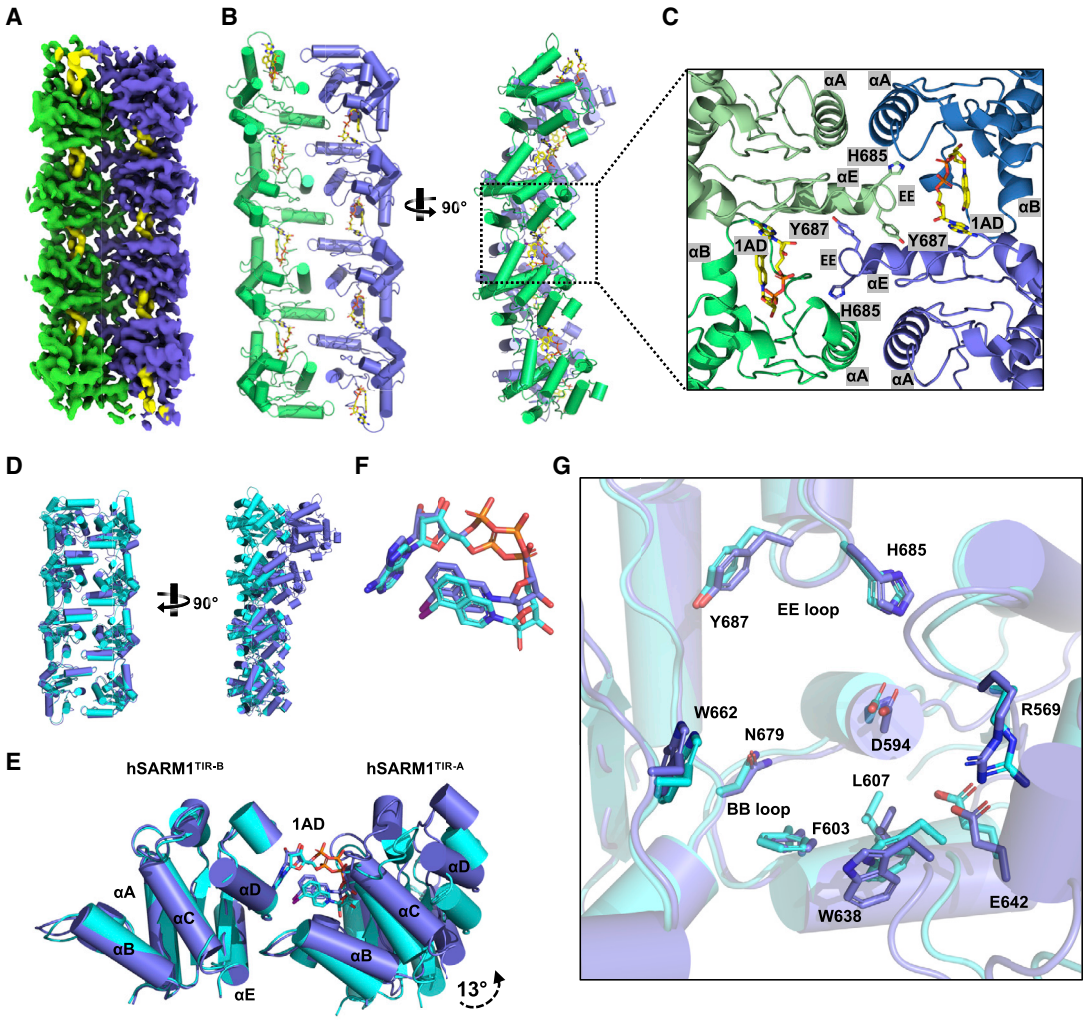

Figure 5. Cryo-EM structure of hSARM1 TIR:1AD

(A) Electrostatic potential density map of the two-stranded TIR domain assembly. The two antiparallel strands are shown in green and slate, respectively. **1AD** is shown in yellow.

(B) Cartoon diagram of the two-stranded TIR domain assembly (helices are depicted as cylinders).

(C) Enlarged cutaway of the TIR domain interfaces in the two-stranded assembly. **1AD** and EE loop residues H685 and Y687 are highlighted in stick representation.

(D–G) Comparison of the TIR-domain assemblies in the hSARM1^{TIR}:**1AD** crystal (cyan) and hSARM1 TIR:**1AD** cryo-EM (slate) structures. (D) Top- (left) and side-view (right) of octameric assembly. (E) Orthosteric site. (F) Zoomed-in view of isolated **1AD** from the orthosteric site. (G) Orthosteric site with residues involved in **1AD** binding highlighted in stick representation. The hSARM1^{TIR-B} chain was used for the alignments in (E–G).

See also Figures S3, S4, and S6.

DISCUSSION

We describe the mechanism of inhibition by a potent and selective orthosteric SARM1 inhibitor (Figure 1) that highlights a base-exchange reaction to generate the *bona fide* inhibitor *in situ*. Several NAD^+ consuming enzymes can catalyze reactions exchanging the NAM moiety of NAD^+ with nucleophilic bases such as heterocyclic amines (CD38, *Aplysia* ADP-ribosyl cyclase, and porcine brain NADase), aliphatic alcohols (porcine brain NADase), and peptides containing Nε-thioacetyl-lysine (sirtuin-1) (Fatkins et al., 2006; Preugschat et al., 2008; Stein et al., 1959; Tonooka and Azuma, 1991, 1994, 1996, 1997, 1999; Tonooka et al., 1977; Zatman et al., 1954). However, the majority of bases able to undergo SARM1 catalyzed base-exchange reactions (Table S2) are different to these previously reported compounds, suggesting that SARM1 has different substrate preferences for base-exchange reactions, consistent with the good target selectivity of **1AD** (Hughes et al., 2021). One possible physiological function of SARM1 base-exchange activity is the conversion of NADP to the strong calcium mobilising agent nicotinic acid adenine dinucleotide phosphate via the exchange of NAM with nicotinic acid (Angeletti et al., 2022; Zhao et al., 2019).

We report active state SARM1 structures in complex with an inhibitor (Figures 2 and 5), substrate mimetics (Figure 3) and

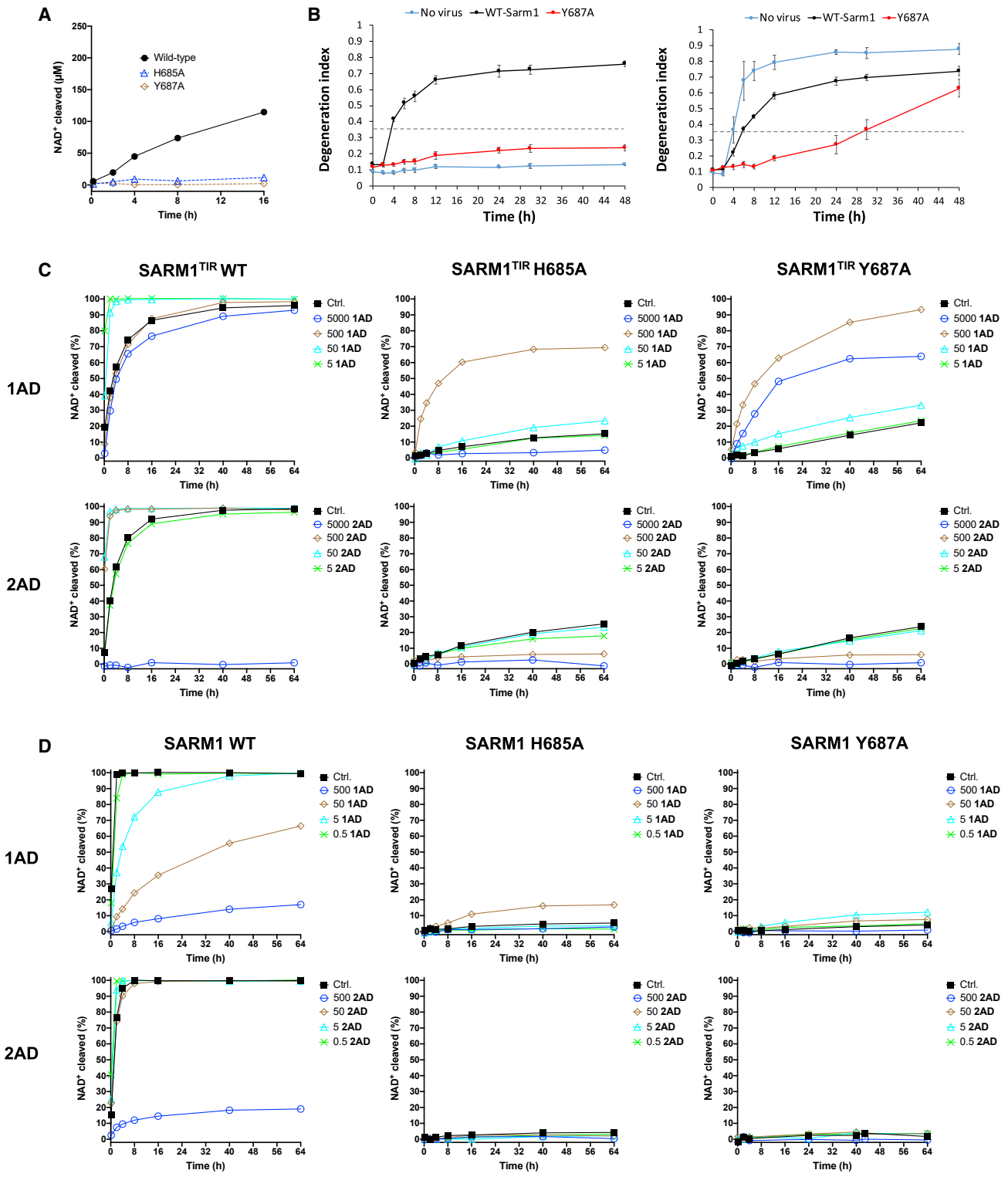

Figure 6. Characterization of EE loop mutants

(A) NADase activities of 0.5 μM wild-type, H685A, and Y687A hSARM1. The initial NAD^+ concentration was 500 μM.

(B) DRG cultures from SARM1 knock out mice (left) or wild-type mice (right) were infected at two days in culture with lentivirus expressing either wild-type SARM1 or the SARM1 Y687A mutant. Axotomy was performed in mature DRG neurons. Axon degeneration was monitored by the axon

(legend continued on next page)

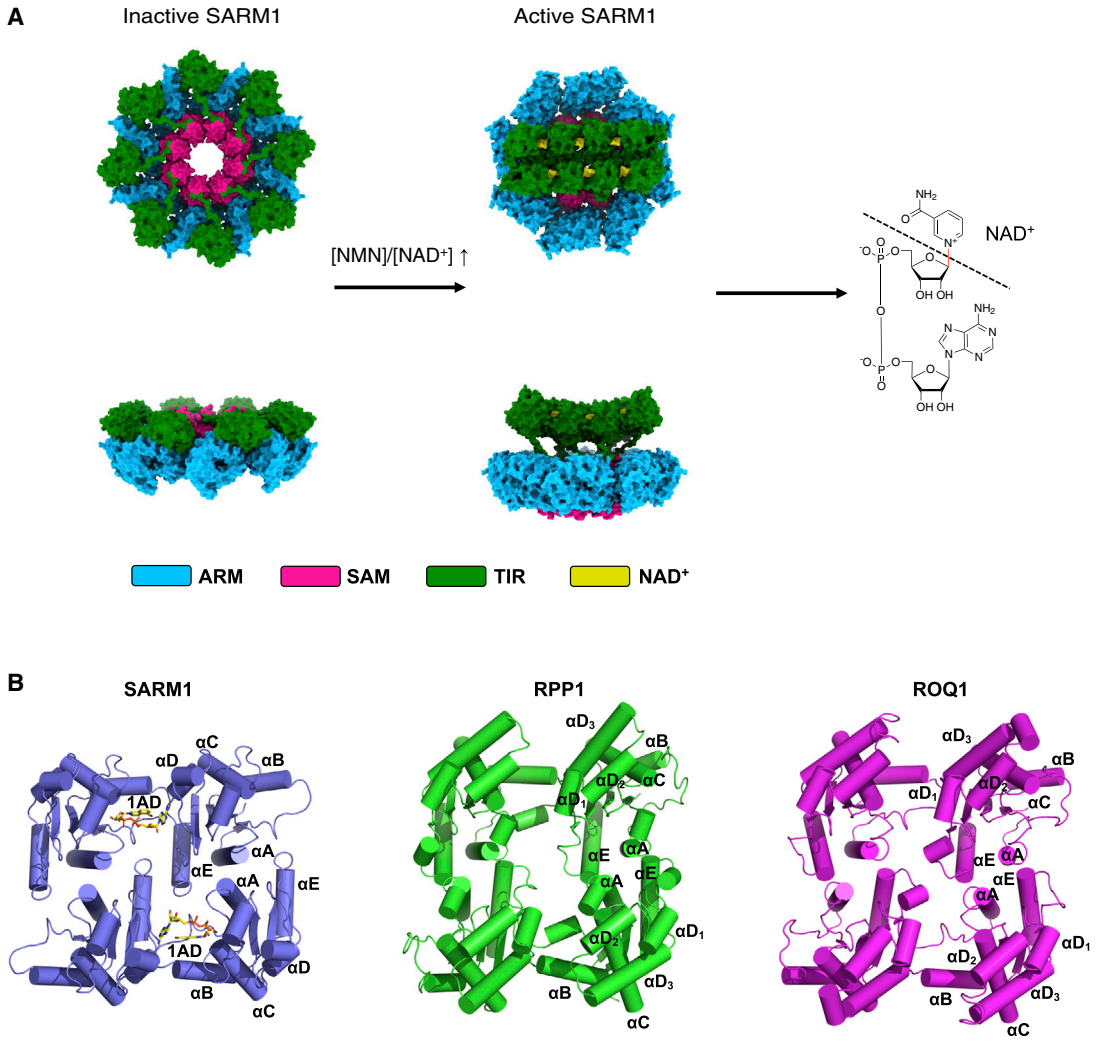

Figure 7. SARM1 activation mechanism

(A) Upon NMN binding, conformational changes in the ARM domain result in their rotation relative to the octameric SAM domain ring, which in turn causes a clash with the TIR domains. As the TIR domains are released from the ring, they self-associate into a two-stranded antiparallel assembly to yield six catalytically-competent active sites per SARM1 octamer. Inactive structure corresponds to PDB: 7ANW. The flexible region between the SAM and TIR domain (residues 546-560) in the activated structure was modeled using Coot.

(B) Comparison of the TIR domain tetramers observed in the RPP1 (PDB: 7JLX) and ROQ1 (PDB: 7DFV) cryo-EM structures with the TIR-domain assembly observed in SARM1.

the allosteric activator NMN (Figure 4). The structures support our recently proposed SARM1 activation model (Figley et al., 2021), and further explain the mechanism of how NMN binding triggers SARM1 activation. In the inactive state, the ARM domains keep the TIR domains apart, and the catalytic sites are not fully formed. Upon NMN binding, conformational changes in the ARM domain result in their rotation relative to the octameric SAM domain ring, which in turn causes a clash with the TIR domains (Figures 4D–4F and Video S1). As the TIR domains are released from the ring, they self-associate into an open-ended assembly with a different symmetry compared to the octameric ring, yielding up to six catalytically-competent active sites per SARM1 octamer (Figure 7A).

Self-association through the BB and EE loop interfaces results in a reorientation of the BB-loop, leading to an active

degeneration index (Gerdts et al., 2013) over time. Results are mean ± SD, n = 3. Axons with index values above 0.35 (dashed line) are considered degenerated.

(C and D) Effects of **1AD** and **2AD** on enzymatic activity. (C) 10 μM wild-type, H685A, and Y87A hSARM1^{TIR} with varying concentrations of **1AD** and **2AD**. (D) 0.5 μM wild-type, H685A, and Y87A hSARM1 activated by 100 min pre-incubation of 500 μM NMN with varying concentrations of **1AD** and **2AD**. The initial concentration of NAD^+ was 500 μM. Concentrations of **1AD** and **2AD** are labeled (μM).

site spanning two TIR-domain monomers. Such formation of active sites is required for both NADase and base-exchange activities of SARM1. We previously observed that K597 can insert into the active site in a hSARM1^{TIR} mutant (G601P) structure, which provided a mechanism for how substrate binding could be blocked in the inactive state (Horsefield et al., 2019). However, this conformation is not observed in the inactive cryo-EM structures (Bratkowski et al., 2020; Figley et al., 2021; Jiang et al., 2020; Shen et al., 2021; Sporny et al., 2020). In these structures, the BB loop region is partially disordered, suggesting that lack of order in the active site region may play a large role in preventing substrate binding.

TIR domain assemblies with a BB-loop mediated asymmetric interfaces analogous to those observed in SARM1 have recently been reported for two plant TIR domain-containing immune receptors with NADase activity, ROQ1 and RPP1 (Ma et al., 2020; Martin et al., 2020) (Figure 7B), suggesting that this is a common active site architecture among eukaryotic TIR domain-containing NADases. However, both plant and bacterial TIR domains have been reported to produce a different set of nucleotide products (ADPR and variant-cADPRs) upon NAD$^+$ cleavage (Eastman et al., 2022; Essuman et al., 2018; Ofir et al., 2021; Wan et al., 2019) compared to SARM1 (ADPR and cADPR) (Essuman et al., 2017; Zhao et al., 2019), suggesting that the mechanistic details of NAD$^+$ cleavage and product formation may vary among TIR domain-containing NADases.

Importantly, our results provide the structural basis for multiple potential avenues to develop therapeutic strategies for hSARM1 inhibition. The enzyme-catalyzed formation of **1AD** represents a distinctive example of *in situ* generated potent inhibitors, which has only recently been described for sirtuin-2, a histone deacetylase that requires NAD$^+$ for its catalytic activity (Mellini et al., 2017). Such enzyme-catalyzed *in situ* generation of ligands could be further leveraged to develop new inhibitors of SARM1, as the catalytic site sits at the BB-loop mediated self-association interface and may possess flexibility to accommodate larger or different pro-drug bases, leading to stronger affinity and inhibition. In addition, preventing the activator NMN from binding at the allosteric site (Figley et al., 2021; Li et al., 2021) via NMN-competitive binders could lead to strong inhibition of hSARM1 activity. Other strategies that prevent reorientation of the ARM domains or block the formation of the two-stranded TIR-domain assemblies could also affect enzyme activity. Therefore, we expect our results to greatly assist in the discovery and development of next-generation SARM1 inhibitors for axon protection.

Limitations of the study

One limitation of our study is the lack of biophysical interaction data (affinity constants and association/dissociation rate constants) for hSARM1 with inhibitors and substrate mimetics. The ability of the hSARM1 TIR domain to form open ended assemblies that can be stabilized by inhibitors (**1AD**), substrate mimetics (**2AD**, **3AD**) or high local protein concentration leads to formation of heterogenous populations of large aggregates of both full-length hSARM1 and hSARM1^{TIR}, which is problematic for biophysical measurements that rely on a constant binding-site concentration in the presence of varying ligand concentrations. An additional limitation of the study is that we were not able to obtain a structure of the hSARM1 TIR domain in complex with NAD$^+$.

STAR★METHODS

Detailed methods are provided in the online version of this paper and include the following:

- KEY RESOURCES TABLE
- RESOURCE AVAILABILITY
  - Lead Contact
  - Materials availability
  - Data and code availability
- EXPERIMENTAL MODEL AND SUBJECT DETAILS
  - Expression of hSARM1^{TIR} in *E. coli*
  - Expression of hSARM1 in HEK293T cells
  - Primary DRG cultures for SARM1 dependent production of 1AD and 3AD and for quantification of axon degeneration by the SARM1 Y687A mutant
  - Primary DRG cultures for production of 1AD and 2AD in axotomized neurons
- METHOD DETAILS
  - Site directed mutagenesis
  - Purification of hSARM1^{TIR}
  - Purification of hSARM1
  - ^{1}H NMR NADase assays
  - Production and purification of base-exchange products
  - Characterization of base-exchange products
  - Enzyme kinetics
  - NADase inhibition assay
  - Analytical size-exclusion chromatography
  - Crystallization and crystal structure determination
  - Cryo-EM sample preparation and data collection
  - Cryo-EM data processing
  - Model building and refinement of hSARM1 cryo-EM structures
  - Structural analyses
  - SARM1-dependent production of **1AD** and **3AD** in DRG neurons
  - Production of 1AD and 2AD in axotomized DRG neurons
  - Axotomy and quantification of axon degeneration for the SARM1 Y687A mutant
- QUANTIFICATION AND STATISTICAL ANALYSIS

SUPPLEMENTAL INFORMATION

Supplemental information can be found online at https://doi.org/10.1016/j.molcel.2022.03.007.

ACKNOWLEDGMENTS

We acknowledge use of the Australian Synchrotron MX facility and thank the staff for their support. We acknowledge the support and use of the Krios at the Midlands Regional Cryo-EM Facility, Institute of Structural and Chemical Biology, University of Leicester, UK. We also acknowledge the Centre for

Microscopy and Microanalysis, University of Queensland and staff (Bill Close, Matthias Floetenmeyer, Richard Webb and Roger Wepf). The work was supported by the National Health and Medical Research Council (NHMRC grants 1196590 to T.V., 1107804 and 1160570 to B.K., and T.V., 1071659 to B.K., and 1108859 to T.V.), the Australian Research Council (ARC) Future Fellowship (FT200100572) to T.V., the ARC Laureate Fellowship (FL180100109) to B.K., the National Institutes of Health (R01NS087632 to J.M. and A.D.) and Disarm Therapeutics. T.V. received ARC DECRA (DE170100783) funding. Y.Shi was a recipient of Griffith University Postdoctoral Fellowship Scheme. F.K.S. was supported by the University of Queensland Research Training Scholarship.

AUTHOR CONTRIBUTIONS

Conceptualization, T.V., Y. Shi, R.O.H., B.K.; Investigation, T.V., Y. Shi, P.S.K., J.D.N., T.B., Y. Sasaki, R.K., F.K.S., S.E.A., T.M., V.M., X.M., F.R., E.V., M.F., K.C., W.G., Z.L., L.B., M.J.L.; Writing – original draft, T.V., Y. Shi; Writing – review & editing, all authors; Funding acquisition, T.V., R.O.H., B.K.; Resources, T.V. B.K., R.O.H., J.M., A.D.; Supervision, T.V., R.O.H., B.K., J.M., A.D., A.B.

DECLARATION OF INTERESTS

A.D. and J.M. are co-founders, scientific advisory board members, and shareholders of Disarm Therapeutics. B.K. is a shareholder of Disarm Therapeutics. Y. Sasaki and B.K. are consultants to Disarm Therapeutics. B.K. and T.V. receive research funding from Disarm Therapeutics. R.O.H., R.K., and T.B. are employees and shareholders in Disarm Therapeutics. S.E.A., M.F., K.C., A.B., and P.S.K. are employees of Evotec SE. R.O.H., T.B., and A.B. are inventors on a patent related to isoquinoline inhibitors of SARM1 (WO 2019/236879 Al). The authors have no additional competing financial interests.

Received: August 4, 2021
Revised: January 11, 2022
Accepted: March 1, 2022
Published: March 24, 2022

REFERENCES

Afonine, P.V., Grosse-Kunstleve, R.W., Echols, N., Headd, J.J., Moriarty, N.W., Mustyakimov, M., Terwilliger, T.C., Urzhumtsev, A., Zwart, P.H., and Adams, P.D. (2012). Towards automated crystallographic structure refinement with phenix.refine. Acta Crystallogr. D Biol. Crystallogr. *68*, 352–367.

Afonine, P.V., Klaholz, B.P., Moriarty, N.W., Poon, B.K., Sobolev, O.V., Terwilliger, T.C., Adams, P.D., and Urzhumtsev, A. (2018). New tools for the analysis and validation of cryo-EM maps and atomic models. Acta Crystallogr. D Struct. Biol. *74*, 814–840.

Angeletti, C., Amici, A., Gilley, J., Loreto, A., Trapanotto, A.G., Antoniou, C., Merlini, E., Coleman, M.P., and Orsomando, G. (2022). SARM1 is a multi-functional NAD(P)ase with prominent base exchange activity, all regulated by multiple physiologically relevant NAD metabolites. iScience *25*, 103812.

Bepler, T., Morin, A., Rapp, M., Brasch, J., Shapiro, L., Noble, A.J., and Berger, B. (2019). Positive-unlabeled convolutional neural networks for particle picking in cryo-electron micrographs. Nat. Methods *16*, 1153–1160.

Bratkowski, M., Xie, T., Thayer, D.A., Lad, S., Mathur, P., Yang, Y.S., Danko, G., Burdett, T.C., Danao, J., Cantor, A., et al. (2020). Structural and mechanistic regulation of the pro-degenerative NAD hydrolase SARM1. Cell Rep. *32*, 107999.

Chen, S., McMullan, G., Faruqi, A.R., Murshudov, G.N., Short, J.M., Scheres, S.H., and Henderson, R. (2013). High-resolution noise substitution to measure overfitting and validate resolution in 3D structure determination by single particle electron cryomicroscopy. Ultramicroscopy *135*, 24–35.

Chen, V.B., Arendall, W.B., 3rd, Headd, J.J., Keedy, D.A., Immormino, R.M., Kapral, G.J., Murray, L.W., Richardson, J.S., and Richardson, D.C. (2010). MolProbity: all-atom structure validation for macromolecular crystallography. Acta Crystallogr. D Biol. Crystallogr. *66*, 12–21.

Clabbers, M.T.B., Holmes, S., Muusse, T.W., Vajjhala, P.R., Thygesen, S.J., Malde, A.K., Hunter, D.J.B., Croll, T.I., Flueckiger, L., Nanson, J.D., et al. (2021). MyD88 TIR domain higher-order assembly interactions revealed by microcrystal electron diffraction and serial femtosecond crystallography. Nat. Commun. *12*, 2578.

Coleman, M.P., and Höke, A. (2020). Programmed axon degeneration: from mouse to mechanism to medicine. Nat. Rev. Neurosci. *21*, 183–196.

Croll, T.I. (2018). ISOLDE: a physically realistic environment for model building into low-resolution electron-density maps. Acta Crystallogr. D Struct. Biol. *74*, 519–530.

Di Stefano, M., Nascimento-Ferreira, I., Orsomando, G., Mori, V., Gilley, J., Brown, R., Janeckova, L., Vargas, M.E., Worrell, L.A., Loreto, A., et al. (2015). A rise in NAD precursor nicotinamide mononucleotide (NMN) after injury promotes axon degeneration. Cell Death Differ. *22*, 731–742.

Eastman, S., Smith, T., Zaydman, M.A., Kim, P., Martinez, S., Damaraju, N., DiAntonio, A., Milbrandt, J., Clemente, T.E., Alfano, J.R., and Guo, M. (2022). A phytobacterial TIR domain effector manipulates NAD^+ to promote virulence. New Phytol. *233*, 890–904.

Emsley, P., and Cowtan, K. (2004). Coot: model-building tools for molecular graphics. Acta Crystallogr. D Biol. Crystallogr. *60*, 2126–2132.

Essuman, K., Summers, D.W., Sasaki, Y., Mao, X., DiAntonio, A., and Milbrandt, J. (2017). The SARM1 Toll/interleukin-1 receptor domain possesses intrinsic NAD^+ cleavage activity that promotes pathological axonal degeneration. Neuron *93*, 1334–1343.e5.

Essuman, K., Summers, D.W., Sasaki, Y., Mao, X., Yim, A.K.Y., DiAntonio, A., and Milbrandt, J. (2018). TIR domain proteins are an ancient family of NAD(+)-consuming enzymes. Curr. Biol. *28*, 421–430.e4.

Evans, P. (2006). Scaling and assessment of data quality. Acta Crystallogr. D Biol. Crystallogr. *62*, 72–82.

Evans, P.R., and Murshudov, G.N. (2013). How good are my data and what is the resolution? Acta Crystallogr. D Biol. Crystallogr. *69*, 1204–1214.

Fatkins, D.G., Monnot, A.D., and Zheng, W. (2006). Nepsilon-thioacetyl-lysine: a multi-facet functional probe for enzymatic protein lysine Nepsilon-deacetylation. Bioorg. Med. Chem. Lett. *16*, 3651–3656.

Figley, M.D., Gu, W., Nanson, J.D., Shi, Y., Sasaki, Y., Cunnea, K., Malde, A.K., Jia, X., Luo, Z., Saikot, F.K., et al. (2021). SARM1 is a metabolic sensor activated by an increased NMN/NAD^+ ratio to trigger axon degeneration. Neuron *109*, 1118–1136.e11.

Geisler, S., Doan, R.A., Strickland, A., Huang, X., Milbrandt, J., and DiAntonio, A. (2016). Prevention of vincristine-induced peripheral neuropathy by genetic deletion of SARM1 in mice. Brain *139*, 3092–3108.

Geisler, S., Huang, S.X., Strickland, A., Doan, R.A., Summers, D.W., Mao, X., Park, J., DiAntonio, A., and Milbrandt, J. (2019). Gene therapy targeting SARM1 blocks pathological axon degeneration in mice. J. Exp. Med. *216*, 294–303.

Gerdts, J., Brace, E.J., Sasaki, Y., DiAntonio, A., and Milbrandt, J. (2015). SARM1 activation triggers axon degeneration locally via NAD^+ destruction. Science *348*, 453–457.

Gerdts, J., Summers, D.W., Sasaki, Y., DiAntonio, A., and Milbrandt, J. (2013). Sarm1-mediated axon degeneration requires both SAM and TIR interactions. J. Neurosci. *33*, 13569–13580.

Goddard, T.D., Huang, C.C., Meng, E.C., Pettersen, E.F., Couch, G.S., Morris, J.H., and Ferrin, T.E. (2018). UCSF ChimeraX: Meeting modern challenges in visualization and analysis. Protein Sci. *27*, 14–25.

Hayward, S., Kitao, A., and Berendsen, H.J. (1997). Model-free methods of analyzing domain motions in proteins from simulation: a comparison of normal mode analysis and molecular dynamics simulation of lysozyme. Proteins *27*, 425–437.

Heightman, T.D., and Vasella, A.T. (1999). Recent insights into inhibition, structure, and mechanism of configuration-retaining glycosidases. Angew. Chem. Int. Ed. Engl. *38*, 750–770.

Henninger, N., Bouley, J., Sikoglu, E.M., An, J., Moore, C.M., King, J.A., Bowser, R., Freeman, M.R., and Brown, R.H., Jr. (2016). Attenuated traumatic axonal injury and improved functional outcome after traumatic brain injury in mice lacking Sarm1. Brain *139*, 1094–1105.

Hopkins, A.L., Groom, C.R., and Alex, A. (2004). Ligand efficiency: a useful metric for lead selection. Drug Discov. Today *9*, 430–431.

Hopkins, A.L., Keserü, G.M., Leeson, P.D., Rees, D.C., and Reynolds, C.H. (2014). The role of ligand efficiency metrics in drug discovery. Nat. Rev. Drug Discov. *13*, 105–121.

Horsefield, S., Burdett, H., Zhang, X., Manik, M.K., Shi, Y., Chen, J., Qi, T., Gilley, J., Lai, J.S., Rank, M.X., et al. (2019). NAD^+ cleavage activity by animal and plant TIR domains in cell death pathways. Science *365*, 793–799.

Hughes, R.O., Bosanac, T., Mao, X., Engber, T.M., DiAntonio, A., Milbrandt, J., Devraj, R., and Krauss, R. (2021). Small molecule SARM1 inhibitors recapitulate the SARM1(−/−) phenotype and allow recovery of a metastable pool of axons fated to degenerate. Cell Rep. *34*, 108588.

Jiang, Y., Liu, T., Lee, C.H., Chang, Q., Yang, J., and Zhang, Z. (2020). The NAD^+-mediated self-inhibition mechanism of pro-neurodegenerative SARM1. Nature *588*, 658–663.

Jubb, H.C., Higueruelo, A.P., Ochoa-Montaño, B., Pitt, W.R., Ascher, D.B., and Blundell, T.L. (2017). Arpeggio: A web server for calculating and visualising interatomic interactions in protein structures. J. Mol. Biol. *429*, 365–371.

Kabsch, W. (2010). XDS. Acta Crystallogr. D Biol. Crystallogr. *66*, 125–132.

Kidmose, R.T., Juhl, J., Nissen, P., Boesen, T., Karlsen, J.L., and Pedersen, B.P. (2019). *Namdinator* - automatic molecular dynamics flexible fitting of structural models into cryo-EM and crystallography experimental maps. IUCrJ *6*, 526–531.

Ko, K.W., Milbrandt, J., and DiAntonio, A. (2020). SARM1 acts downstream of neuroinflammatory and necroptotic signaling to induce axon degeneration. J. Cell Biol. *219*, e201912047.

Koshland, D.E., Jr. (1953). Stereochemistry and the mechanism of enzymatic reactions. Biol. Rev. Camb. Philos. Soc. *28*, 416–436.

Krauss, R., Bosanac, T., Devraj, R., Engber, T., and Hughes, R.O. (2020). Axons Matter: The Promise of Treating Neurodegenerative Disorders by Targeting SARM1-Mediated Axonal Degeneration. Trends Pharmacol. Sci. *41*, 281–293.

Krissinel, E., and Henrick, K. (2007). Inference of macromolecular assemblies from crystalline state. J. Mol. Biol. *372*, 774–797.

Li, W.H., Huang, K., Cai, Y., Wang, Q.W., Zhu, W.J., Hou, Y.N., Wang, S., Cao, S., Zhao, Z.Y., Xie, X.J., et al. (2021). Permeant fluorescent probes visualize the activation of SARM1 and uncover an anti-neurodegenerative drug candidate. eLife *10*, e67381.

Loreto, A., Di Stefano, M., Gering, M., and Conforti, L. (2015). Wallerian Degeneration Is Executed by an NMN-SARM1-Dependent Late Ca(2+) Influx but Only Modestly Influenced by Mitochondria. Cell Rep. *13*, 2539–2552.

Loring, H.S., Czech, V.L., Icso, J.D., O'Connor, L., Parelkar, S.S., Byrne, A.B., and Thompson, P.R. (2021). A phase transition enhances the catalytic activity of SARM1, an NAD^+ glycohydrolase involved in neurodegeneration. eLife *10*, e66694.

Loring, H.S., and Thompson, P.R. (2020). Emergence of SARM1 as a Potential Therapeutic Target for Wallerian-type Diseases. Cell Chem. Biol. *27*, 1–13.

Ma, S., et al. (2020). Direct pathogen-induced assembly of an NLR immune receptor complex to form a holoenzyme. Science *370*, eabe3069.

Marion, C.M., McDaniel, D.P., and Armstrong, R.C. (2019). Sarm1 deletion reduces axon damage, demyelination, and white matter atrophy after experimental traumatic brain injury. Exp. Neurol. *321*, 113040.

Martin, R., Qi, T., Zhang, H., Liu, F., King, M., Toth, C., Nogales, E., and Staskawicz, B.J. (2020). Structure of the activated ROQ1 resistosome directly recognizing the pathogen effector XopQ. Science *370*, eabd9993.

Maynard, M.E., Redell, J.B., Zhao, J., Hood, K.N., Vita, S.M., Kobori, N., and Dash, P.K. (2020). Sarm1 loss reduces axonal damage and improves cognitive outcome after repetitive mild closed head injury. Exp. Neurol. *327*, 113207.

McCoy, A.J. (2007). Solving structures of protein complexes by molecular replacement with Phaser. Acta Crystallogr. D Biol. Crystallogr. *63*, 32–41.

Mellini, P., Itoh, Y., Tsumoto, H., Li, Y., Suzuki, M., Tokuda, N., Kakizawa, T., Miura, Y., Takeuchi, J., Lahtela-Kakkonen, M., and Suzuki, T. (2017). Potent mechanism-based sirtuin-2-selective inhibition by an *in situ*-generated occupant of the substrate-binding site, "selectivity pocket" and NAD^+-binding site. Chem. Sci. (Camb.) *8*, 6400–6408.

Ofir, G., Herbst, E., Baroz, M., Cohen, D., Millman, A., Doron, S., Tal, N., Malheiro, D.B.A., Malitsky, S., Amitai, G., and Sorek, R. (2021). Antiviral activity of bacterial TIR domains via immune signalling molecules. Nature *600*, 116–120.

Osterloh, J.M., Yang, J., Rooney, T.M., Fox, A.N., Adalbert, R., Powell, E.H., Sheehan, A.E., Avery, M.A., Hackett, R., Logan, M.A., et al. (2012). dSarm/Sarm1 is required for activation of an injury-induced axon death pathway. Science *337*, 481–484.

Pintilie, G.D., Zhang, J., Goddard, T.D., Chiu, W., and Gossard, D.C. (2010). Quantitative analysis of cryo-EM density map segmentation by watershed and scale-space filtering, and fitting of structures by alignment to regions. J. Struct. Biol. *170*, 427–438.

Piotto, M., Saudek, V., and Sklenár, V. (1992). Gradient-tailored excitation for single-quantum NMR spectroscopy of aqueous solutions. J. Biomol. NMR *2*, 661–665.

Preugschat, F., Tomberlin, G.H., and Porter, D.J. (2008). The base exchange reaction of NAD+ glycohydrolase: identification of novel heterocyclic alternative substrates. Arch. Biochem. Biophys. *479*, 114–120.

Punjani, A., Rubinstein, J.L., Fleet, D.J., and Brubaker, M.A. (2017). cryoSPARC: algorithms for rapid unsupervised cryo-EM structure determination. Nat. Methods *14*, 290–296.

Punjani, A., Zhang, H., and Fleet, D.J. (2020). Non-uniform refinement: adaptive regularization improves single-particle cryo-EM reconstruction. Nat. Methods *17*, 1214–1221.

Rosenthal, P.B., and Henderson, R. (2003). Optimal determination of particle orientation, absolute hand, and contrast loss in single-particle electron cryomicroscopy. J. Mol. Biol. *333*, 721–745.

Sasaki, Y., Engber, T.M., Hughes, R.O., Figley, M.D., Wu, T., Bosanac, T., Devraj, R., Milbrandt, J., Krauss, R., and DiAntonio, A. (2020). cADPR is a gene dosage-sensitive biomarker of SARM1 activity in healthy, compromised, and degenerating axons. Exp. Neurol. *329*, 113252.

Sasaki, Y., Nakagawa, T., Mao, X., DiAntonio, A., and Milbrandt, J. (2016). NMNAT1 inhibits axon degeneration via blockade of SARM1-mediated NAD^+ depletion. eLife *5*, e19749.

Sasaki, Y., Vohra, B.P.S., Lund, F.E., and Milbrandt, J. (2009). Nicotinamide mononucleotide adenylyl transferase-mediated axonal protection requires enzymatic activity but not increased levels of neuronal nicotinamide adenine dinucleotide. J. Neurosci. *29*, 5525–5535.

Scheres, S.H. (2012). RELION: implementation of a Bayesian approach to cryo-EM structure determination. J. Struct. Biol. *180*, 519–530.

Scheres, S.H., and Chen, S. (2012). Prevention of overfitting in cryo-EM structure determination. Nat. Methods *9*, 853–854.

Shen, C., Vohra, M., Zhang, P., Mao, X., Figley, M.D., Zhu, J., Sasaki, Y., Wu, H., DiAntonio, A., and Milbrandt, J. (2021). Multiple domain interfaces mediate SARM1 autoinhibition. Proc. Natl. Acad. Sci. USA *118*, e2023151118.

Sklenar, V., Piotto, M., Leppik, R., and Saudek, V. (1993). Gradient-tailored water suppression for 1H-15N HSQC experiments optimized to retain full sensitivity. J. Magn. Reson. *102*, 241–245.

Sporny, M., Guez-Haddad, J., Khazma, T., Yaron, A., Dessau, M., Shkolnisky, Y., Mim, C., Isupov, M.N., Zalk, R., Hons, M., and Opatowsky, Y. (2020). Structural basis for SARM1 inhibition and activation under energetic stress. eLife *9*, e62021.

Sporny, M., Guez-Haddad, J., Lebendiker, M., Ulisse, V., Volf, A., Mim, C., Isupov, M.N., and Opatowsky, Y. (2019). Structural evidence for an octameric ring arrangement of SARM1. J. Mol. Biol. *431*, 3591–3605.

Stein, A.M., Kaplan, N.O., and Ciotti, M.M. (1959). Pyridine nucleotide transhydrogenase. VII. Determination of the reactions with coenzyme analogues in mammalian tissues. J. Biol. Chem. *234*, 979–986.

Studier, F.W. (2005). Protein production by auto-induction in high density shaking cultures. Protein Expr. Purif. *41*, 207–234.

Szretter, K.J., Samuel, M.A., Gilfillan, S., Fuchs, A., Colonna, M., and Diamond, M.S. (2009). The immune adaptor molecule SARM modulates tumor necrosis factor alpha production and microglia activation in the brainstem and restricts West Nile Virus pathogenesis. J. Virol. *83*, 9329–9338.

Tonooka, S., and Azuma, I. (1991). Enzymatic preparations and regiochemical properties of some new Adp-ribosylated 1,2,4-Triazoles. Gazz. Chim. Ital. *121*, 297–300.

Tonooka, S., and Azuma, I. (1994). Evidence for enzymatic Adp-ribosylation to histidine and related dipeptides. Acta Chem. Scand. *48*, 780–782.

Tonooka, S., and Azuma, I. (1996). Triazolo[4,5-b]- and imidazo[4,5-b]pyridines as substrates of NAD glycohydrolase: Evidence for two competitive transglycosylation reaction sites. Liebigs Ann. *1996*, 863–865.

Tonooka, S., and Azuma, I. (1997). Enzymatic alcoholyses of NAD: A new type of ADP-ribosylation reaction catalysed by NAD glycohydrolase. Liebigs Ann. *1997*, 1823–1826.

Tonooka, S., and Azuma, I. (1999). Terminal diols as efficient substrates for transglycosylational activity of NAD glycohydrolase. Nucleosides Nucleotides *18*, 39–49.

Tonooka, S., Sasaki, A., Shirahama, H., Matsumoto, T., and Kakimoto, S. (1977). Enzymatic-synthesis of clitidine. Chem. Lett. *6*, 1449–1452.

Turkiew, E., Falconer, D., Reed, N., and Höke, A. (2017). Deletion of Sarm1 gene is neuroprotective in two models of peripheral neuropathy. J. Peripher. Nerv. Syst. *22*, 162–171.

Ve, T., Vajjhala, P.R., Hedger, A., Croll, T., DiMaio, F., Horsefield, S., Yu, X., Lavrencic, P., Hassan, Z., Morgan, G.P., et al. (2017). Structural basis of TIR-domain-assembly formation in MAL- and MyD88-dependent TLR4 signaling. Nat. Struct. Mol. Biol. *24*, 743–751.

Wan, L., Essuman, K., Anderson, R.G., Sasaki, Y., Monteiro, F., Chung, E.H., Osborne Nishimura, E., DiAntonio, A., Milbrandt, J., Dangl, J.L., and Nishimura, M.T. (2019). TIR domains of plant immune receptors are NAD^+-cleaving enzymes that promote cell death. Science *365*, 799–803.

Williams, C.J., Headd, J.J., Moriarty, N.W., Prisant, M.G., Videau, L.L., Deis, L.N., Verma, V., Keedy, D.A., Hintze, B.J., Chen, V.B., et al. (2018). MolProbity: More and better reference data for improved all-atom structure validation. Protein Sci. *27*, 293–315.

Wu, T., Zhu, J., Strickland, A., Ko, K.W., Sasaki, Y., Dingwall, C.B., Yamada, Y., Figley, M.D., Mao, X., Neiner, A., et al. (2021). Neurotoxins subvert the allosteric activation mechanism of SARM1 to induce neuronal loss. Cell Rep. *37*, 109872.

Zatman, L.J., Kaplan, N.O., Colowick, S.P., and Ciotti, M.M. (1954). Effect of isonicotinic acid hydrazide on diphosphopyridine nucleotidases. J. Biol. Chem. *209*, 453–466.

Zechel, D.L., and Withers, S.G. (2000). Glycosidase mechanisms: anatomy of a finely tuned catalyst. Acc. Chem. Res. *33*, 11–18.

Zhang, K. (2016). Gctf: Real-time CTF determination and correction. J. Struct. Biol. *193*, 1–12.

Zhao, Z.Y., et al. (2019). A cell-permeant mimetic of NMN activates SARM1 to produce cyclic ADP-Ribose and induce non-apoptotic cell death. iScience *15*, 452–466.

Ziogas, N.K., and Koliatsos, V.E. (2018). Primary traumatic axonopathy in mice subjected to impact acceleration: a reappraisal of pathology and mechanisms with high-resolution anatomical methods. J. Neurosci. *38*, 4031–4047.

STAR★METHODS

KEY RESOURCES TABLE

REAGENT or RESOURCE	SOURCE	IDENTIFIER
Bacterial and virus strains		
NEB 5-alpha competent cells	New England Biolabs	Cat# C2987I
BL21 (DE3) competent cells	Sigma Aldrich	Cat# 69450-3
Chemicals, peptides, and recombinant proteins		
β-nicotinamide mononucleotide (NMN)	Sigma Aldrich	Cat# N3501
β-nicotinamide adenine dinucleotide sodium salt (NAD^+)	Sigma Aldrich	Cat# N0632
B-27 Supplement (50X), serum free	Thermo-Fisher	Cat# 17504044
Nerve Growth Factor (NGF)	Envigo Bioproducts	Cat# B.5017
5-Fluoro-2'-deoxyuridine	Sigma-Aldrich	Cat# F0503
Uridine	Sigma-Aldrich	Cat# U3003
Poly-D-lysine hydrobromide	Sigma-Aldrich	Cat# P0899
Laminin Mouse Protein	Thermo-Fisher	Cat# 23017015
Citrate	Sigma Aldrich	Cat# S4641
1 (DSRM-3716; 5-iodoisoquinoline)	Hughes et al., 2021	N/A
araF-NAD^+	Biolog g Life Science Institute GmbH & Co	D 148-005
2 (1,2-Dihydro-2,7-naphthyridin-1-one)	Enamine	EN300-176725
3 (8-aminoisoquinoline)	Enamine	EN300-102226
1AD	This study	N/A
2AD	This study	N/A
3AD	This study	N/A
4 (1,2,3,4-tetrahydro-2,7-naphthyridin-1-one)	This study	N/A
5 (4-bromo-1,2-dihydro-2,7-naphthyridin-1-one)	This study	N/A
6 (5-bromoisoquinoline)	Hughes et al., 2021	N/A
7 (3-iodo-1H-pyrrolo[2,3-c]pyridine)	Enamine	EN300-1699504
8 (Thionicotinamide)	Enamine	EN300-17569
9 (5,6-dihydro-1,6-naphthyridin-5-one)	Enamine	EN300-88515
10 (2,7-Naphthyridin-1-amine)	Enamine	EN300-177078
11 3-(1H-imidazol-2-yl)pyridine	Enamine	EN300-61048
12 (Pyridine)	Sigma Aldrich	Cat# 270407
13 (3-Aminopyridine)	Sigma Aldrich	Cat# A78209
14 (4-Phenylpyridine)	Sigma Aldrich	Cat# P33429
15 (Pyrrole)	Sigma Aldrich	Cat# 131709
16 (Imidazole)	Sigma Aldrich	Cat# 56750
17 (Thiazole)	Sigma Aldrich	Cat# 151645
18 (Pyridazine)	Sigma Aldrich	Cat# P57204
19 (Pyrimidine)	Sigma Aldrich	Cat# 131695
20 (Pyrazine)	Sigma Aldrich	Cat# P56003
21 (Piperdine)	Sigma Aldrich	Cat# 411027
22 (Morpholine)	Sigma Aldrich	Cat# 394467
23 (Indole)	Sigma Aldrich	Cat# I3408
24 (5-bromophthalazine)	Sigma Aldrich	Cat# CDS021144
25 (Isoniazid)	Sigma Aldrich	Cat# I3377
26 (Histidine)	Sigma Aldrich	Cat# H0750000
27 (5-aminoisoquinoline)	This study	N/A

(*Continued on next page*)

Continued

REAGENT or RESOURCE	SOURCE	IDENTIFIER
28 (5-chloroisoquinoline)	This study	N/A
29 (5-bromo-3-methylisoquinoline)	This study	N/A
30 (5-bromo-1-methylisoquinoline)	This study	N/A
31 (5-bromo-4-methylisoquinoline)	This study	N/A
32 (5-bromoisoquinolin-6-amine)	This study	N/A
33 (5-bromo-7-methoxyisoquinoline)	This study	N/A
34 (5-bromo-8-methoxyisoquinoline)	This study	N/A
35 (1-iodonaphthalene)	Sigma Aldrich	Cat# 238139
$hSARM1_{28-724}$	Figley et al., 2021	N/A
$hSARM1^{TIR}$ (residues 561-700)	Horsefield et al., 2019	N/A
hSARM1 F603A	This study	N/A
$hSARM1^{TIR}$ F603A	This study	N/A
hSARM1 W638A	This study	N/A
$hSARM1^{TIR}$ W638A	Horsefield et al., 2019	N/A
hSARM1 W662A	This study	N/A
$hSARM1^{TIR}$ W662A	This study	N/A
hSARM1 N679A	This study	N/A
$hSARM1^{TIR}$ N679A	This study	N/A
hSARM1 H685A	This study	N/A
$hSARM1^{TIR}$ H685A	Horsefield et al., 2019	N/A
hSARM1 Y687A	This study	N/A
$hSARM1^{TIR}$ Y687A	This study	N/A
STREP-TEV-$hSARM1^{409-700}$	Hughes et al., 2021	N/A
Deposited data		
Structure of the activated Roq1 resistosome directly recognizing the pathogen effector XopQ	Martin et al., 2020	PDB: 7JLX
Cryo-EM structure of plant NLR RPP1 tetramer core part	Ma et al., 2020	PDB: 7DVF
Crystal structure of the TIR domain from human SARM1 in complex with ribose	Horsefield et al., 2019	PDB: 6O0Q
Crystal structure of the TIR domain from human SARM1 in complex with glycerol	Horsefield et al., 2019	PDB: 6O0R
Ligand-free $hSARM1_{28-724}$ cryo-EM structure	Figley et al., 2021	PDB: 7LD0
NMN bound $dSARM^{ARM}$ crystal structure	Figley et al., 2021	PDB: 7LCZ
hSARM1 NAD+ complex	Sporny et al., 2020	PDB: 7ANW
$hSARM^{TIR}$ **1AD** complex	This paper	PDB: 7NAG
$hSARM^{TIR}$ **2AD** complex	This paper	PDB: 7NAH
$hSARM^{TIR}$ **3AD** complex	This paper	PDB: 7NAI
$hSARM^{TIR}$ araF-ADPR complex	This paper	PDB: 7NAJ
hSARM1 TIR:**1AD** cryoEM map and model	This paper	EMDB: EMD-24272 and PDB: 7NAK
hSARM1 ARM-SAM:NMN cryoEM map and model	This paper	EMDB: EMD-24273 and PDB: 7NAL
hSARM1 SAM-TIR:**1AD** cryoEM map	This paper	EMDB: EMD-24274
$hSARM1^{TIR}$:**1AD** cryoEM map	This paper	EMDB: EMD-26191
Experimental models: Cell lines		
HEK293S	ATCC	Cat# CRL-3022
Experimental models: Organisms/strains		
Mouse: CD-1	Charles River Laboratories	Crl:CD1 (ICR)
Mouse: *Sarm1*$^{-/-}$	Szretter et al., 2009	N/A
Mouse: C57BL/6J	Janvier labs	RRID:IMSR_JAX:000664

(*Continued on next page*)

Continued

REAGENT or RESOURCE	SOURCE	IDENTIFIER
Recombinant DNA		
PSF-CMV-AMP His_6Tag-TEV-AviTag-hSARM1$_{28-724}$	Figley et al., 2021	N/A
PSF-CMV-AMP His_6Tag-TEV-AviTag-hSARM1$_{28-724}$ (F603A)	This study	N/A
PSF-CMV-AMP His_6Tag-TEV-AviTag-hSARM1$_{28-724}$ (W638A)	This study	N/A
PSF-CMV-AMP His_6Tag-TEV-AviTag-hSARM1$_{28-724}$ (W662A)	This study	N/A
PSF-CMV-AMP His_6Tag-TEV-AviTag-hSARM1$_{28-724}$ (N679A)	This study	N/A
PSF-CMV-AMP His_6Tag-TEV-AviTag-hSARM1$_{28-724}$ (H685A)	This study	N/A
PSF-CMV-AMP His_6Tag-TEV-AviTag-hSARM1$_{28-724}$ (Y687A)	This study	N/A
pMCSG7 His_6Tag-TEV-hSARM1$_{561-700}$	Horsefield et al., 2019	N/A
pMCSG7 His_6Tag-TEV-hSARM1$_{561-700}$ (F603A)	This study	N/A
pMCSG7 His_6Tag-TEV-hSARM1$_{561-700}$ (W638A)	This study	N/A
pMCSG7 His_6Tag-TEV-hSARM1$_{561-700}$ (W662A)	This study	N/A
pMCSG7 His_6Tag-TEV-hSARM1$_{561-700}$ (N679A)	This study	N/A
pMCSG7 His_6Tag-TEV-hSARM1$_{561-700}$ (H685A)	This study	N/A
pMCSG7 His_6Tag-TEV-hSARM1$_{561-700}$ (Y687A)	This study	N/A
STREP-TEV-hSARM1$^{409-700}$	Hughes et al., 2021	N/A
FC SARM1-T2A-P2A-Venus	This paper	N/A
FC SARM1^{Y687A}-T2A-P2A-Venus	This paper	N/A
Software and algorithms		
TopSpin™	Bruker	https://www.bruker.com/products/mr/nmr/software/topspin.html
Mnova 11	Mestrelab Research	https://mestrelab.com/software/mnova
XDS	(Kabsch, 2010)	https://xds.mr.mpg.de/
Aimless	Evans and Murshudov, 2013	https://www.ccp4.ac.uk/
PHENIX	Afonine et al., 2012	https://www.phenix-online.org
Phaser	(McCoy, 2007)	https://www.phenix-online.org
Molprobity	Chen et al., 2010	http://molprobity.biochem.duke.edu/
CryoSPARC (version 3.1)	Punjani et al., 2017	https://cryosparc.com
RELION 3.1	Scheres and Chen, 2012	https://www.ccpem.ac.uk/
GCTF	(Zhang, 2016)	https://www.ccpem.ac.uk/
Topaz	Bepler et al., 2019	http://cb.csail.mit.edu/cb/topaz
Chimera	Pintilie et al., 2010	https://www.cgl.ucsf.edu/chimera
ChimeraX	Goddard et al., 2018	https://www.cgl.ucsf.edu/chimerax
Namdinator	Kidmose et al., 2019	https://namdinator.au.dk
Coot	(Emsley and Cowtan, 2004)	https://www2.mrc-lmb.cam.ac.uk/personal/pemsley/coot
ISOLDE	(Croll, 2018)	https://isolde.cimr.cam.ac.uk/
PyMOL (version 2.2.3)	Schrödinger, LLC	https://pymol.org/2/
Arpeggio	Jubb et al., 2017	http://biosig.unimelb.edu.au/arpeggioweb/
Dyndom	Hayward et al., 1997	http://dyndom.cmp.uea.ac.uk/dyndom/
PISA	Krissinel and Henrick, 2007	https://www.ebi.ac.uk/pdbe/pisa/
Prism	Graph Pad	RRID:SCR_002798
Unicorn 7	Cytiva	https://www.cytivalifesciences.com

(*Continued on next page*)

Continued

REAGENT or RESOURCE	SOURCE	IDENTIFIER
Other		
Histrap FF 5 mL	Cytiva	Cat# 17531901
HiLoad 26/60 Superdex 75 pg	Cytiva	Cat# 28989334
HiLoad 26/60 Superdex 200 pg	Cytiva	Cat# 28989336
SnakeSkin Dialysis Tubing, 3.5K MWCO	Thermofisher	Cat# 68035
Titan Krios microscope	Thermofisher	Product site: https://www.thermofisher.com/au/en/home/electron-microscopy/products/transmission-electron-microscopes.html
Mark IV Vitrobot	Thermofisher	Product site: https://www.thermofisher.com/au/en/home/electron-microscopy/products/sample-preparation-equipment-em.html
GloQube	Quorum Tech	Product site: https://www.quorumtech.com/products/glow-discharge-2/
Quantifoil (Au 400 R.2/2) grids	Quantifoil Micro Tools GmbH, Germanuy	Product site: https://www.quantifoil.com
Quantifoil (Au 300 R1.2/1.3) grids	Quantifoil Micro Tools GmbH, Germanuy	Product site: https://www.quantifoil.com
Bruker Avance 600 MHz NMR spectrometer equipped with $^{1}H/^{13}C/^{15}N$ triple resonance cryoprobe	Bruker	Product site: https://www.bruker.com/products/mr/nmr.html
3 mm unracked NMR-tubes	Bruker	Cat# Z172598
BioSep 3000 column	Phenomenex	CAT# 00H-2146-E0
Diener Femto Plasma Cleaner	Diener Plasma Surface Technology, Ebhausen, Germany	Product site: https://www.plasma.com/en/
CRYO ARM™ 300 microscope	JEOL Ltd, Akishima, Tokyo, Japan	Product site: https://www.jeol.co.jp/en/
Gatan K3 direct electron detector	Gatan, Pleasanton, CA, USA	Product site: https://www.gatan.com/K3
Synergi™ 4 μm Hydro-RP 80 Å column	Phenomenex	CAT # 00G-4375-N0
Kinetex 2.6 μm HILIC, 150 × 2.1 mm	Phenomenex	CAT # 00F-4461-AN
RapidFire 300 Mass Spectrometer	Agilent	Product site: https://www.agilent.com/
API4000 triple quadrupole mass spectrometer	AB Sciex, Framingham, MA	Product site: https://sciex.com/
TSQ Quantiva Triple-Stage Quadrupole Mass Spectrometer	Thermo Electron Corporation, San Jose, CA, USA	Product site: https://www.thermofisher.com
Thermo IonMax ESI probe	Thermo Scientific	Cat# IQLAAEGABBFACTMAJI

RESOURCE AVAILABILITY

Lead Contact

Further information and requests for resources and reagents should be directed to and will be fulfilled by the Lead Contact, Thomas Ve (t.ve@griffith.edu.au).

Materials availability

Some unique/stable reagents may be available from the Lead Contact with a completed Materials Transfer Agreement. Restrictions may apply on some of the reagents due to limited availability and prioritization for internal use.

Data and code availability

- Coordinates for the crystal structures of **1AD**, **2AD**, **3AD** and araF-ADPR bound hSARM^{TIR} have been deposited in the Protein Data Bank (PDB: 7NAG, 7NAH, 7NAI, 7NAJ). The hSARM1 TIR:**1AD** and ARM-SAM:NMN cryo-EM maps and coordinates have been deposited to the Electron Microscopy Data Bank (EMDB: EMD-24272, EMD-24273) and Protein Data Bank (PDB: 7NAK,

7NAL), respectively. The hSARM1 SAM-TIR:**1AD** and hSARM1^{TIR}:**1AD** cryo-EM maps have been deposited to the Electron Microscopy Data Bank (EMDB: EMD-24274, EMD-26191).

- This paper does not report original code.
- Any additional information required to reanalyze the data reported in this paper is available from the lead contact upon request.

EXPERIMENTAL MODEL AND SUBJECT DETAILS

Expression of hSARM1^{TIR} in *E. coli*

hSARM1^{TIR} and mutants (residues 561-700 in pMCSG7, N-terminal His$_6$-tag, TEV-protease cleavage site) (Horsefield et al., 2019) were produced in *E. coli* BL21 (DE3) cells using the autoinduction method (Studier, 2005) and purified to homogeneity using a combination of immobilised metal-ion affinity chromatography (IMAC) and size-exclusion chromatography (SEC). The cells were grown at 37°C, until an OD^{600} of 0.6- 0.8 was reached. The temperature was then reduced to 20°C, and the cells were grown overnight for approximately 16 h. The cells were harvested by centrifugation at 5000 x *g* at 4°C for 15 min, and stored at −80°C until used for purification.

Expression of hSARM1 in HEK293T cells

hSARM1 and mutants (residues 28-724 in PSF-CMV-AMP, N-terminal His$_6$-tag, TEV-protease cleavage site, AVI-tag) (Figley et al., 2021) were expressed in HEK293S cells (ATCC) and purified to homogeneity using a combination of IMAC and SEC. The HEK293S cell experiments were performed in accordance with Griffith University Research Ethics Committee approval 2020/246. The cells (were grown in 50% Freestyle 293 Expression Medium (GIBCO) and 50% Ex-Cell 293 Medium (Sigma) supplemented with 3% L-glutamine in vented flasks at 90 rpm in an 80% humidified, 8% carbon dioxide atmosphere at 37°C. When cells reached a density of 2 × 10^6 cells/mL, they were centrifuged at 500 x *g* for 10 min and resuspended in 100% Freestyle 293 Expression Medium to a density of 2.5 × 10^6 cells/mL. After resuspension the cells were transfected with 3 μg/mL of plasmid DNA using Polyethylenimine (PEI) transfection reagent (Polysciences) and growth was continued overnight. On the next day, transfected cells were diluted 1:1 with Ex-Cell 293 Medium and valproic acid was added to a final concentration of 2.2 mM. Growth was continued for an additional three days. Cells were harvested by centrifugation at 1,500 x *g* for 10 min at 4°C and stored at −80°C until used for purification.

Primary DRG cultures for SARM1 dependent production of 1AD and 3AD and for quantification of axon degeneration by the SARM1 Y687A mutant

All animal experiments were performed in accordance with the policies and guidelines of the Institutional Animal Care and Use Committee (IACUC) of Washington University in St. Louis (specific protocols #20-0020 and #20-0484). DRG neurons were isolated from E13.5 CD1 mouse embryo or *Sarm1*$^{-/-}$ timed pregnant mice (Szretter et al., 2009) and cultured in 24-well culture plate (Corning 3524) coated with poly-D-lysine and laminin with 500 μL of a complete medium (Neurobasal medium, GIBCO) with 2% B27 (Invitrogen), 100 ng/mL 2.5S NGF (Harlan Bioproducts), 1 μM uridine (Sigma), 1 μM 5-fluoro-2'-deoxyuridine (Sigma), and penicillin streptomycin) (Sasaki et al., 2016).

Primary DRG cultures for production of 1AD and 2AD in axotomized neurons

For mouse dorsal root ganglia (DRG) cultures, C57BL/6J RRID:IMSR_JAX:000664, were obtained from Janvier labs (Le Genest-Saint-Isle, FR). All animal experiments were carried out in accordance with the regulations of the German animal welfare act and the directive 2010/63/EU of the European Parliament on the protection of animals used for scientific purposes. Protocols were approved by the local ethics committee of the Authority for Health and Consumer Protection of the city and state Hamburg ('Behörde für Gesundheit und Verbraucherschutz' BGV, Hamburg). Female mice, 10-12 weeks in age were housed on a 12 h light/dark cycle with *ad libitum* access to food and water. DRGs were dissected from embryonic day 13.5 mouse embryos (~50 ganglia per embryo) and incubated with 0.05% (w/v) trypsin solution containing 0.02% (w/v) EDTA at 37°C for 30 min. After 2 min gentle centrifugation trypsin solution was removed and replaced for Neurobasal medium, 10% fetal bovine serum. Then, DRGs were triturated by gentle pipetting, cell suspensions were washed 3 times with DRG growth medium (Neurobasal medium; ThermoFisher) containing 2% B27 (ThermoFisher), 50 ng/mL 2.5S NGF (Sigma), 10 μM uridine (Sigma), 10 μM 5-fluoro-2- deoxyuridine (Sigma), 50 U/mL penicillin, and streptomycin. After the last wash, cells were resuspended in DRG growth medium at a ratio of ~100 μL medium/50 DRGs and counted. The cell density of these suspensions was adjusted to 1x10^7 cells/mL. Cell suspensions were seeded at 100,000 cells/well as a 10 μL spotted culture in the center of 24 well plates coated with poly-D-Lysine (0.1 mg/mL; Sigma) and laminin (3 μg/mL; ThermoFisher), and placed in a humidified CO_2 incubator for 15 min. After allowing for cells to adhere, culture media was added gently to a final well volume of 1 mL/well.

METHOD DETAILS

Site directed mutagenesis

hSARM1^{TIR} and hSARM1 mutants were produced using Q5® Site-Directed Mutagenesis (New England BioLabs). Pure plasmids were prepared using the QIAprep Spin Miniprep Kit (QIAGEN) and the sequences were confirmed by the Australian Genome Research Facility.

Purification of hSARM1^{TIR}

hSARM^{TIR} was expressed as described in the experimental model and subject details section. The cells were harvested by centrifugation at 5000 x *g* at 4°C for 15 min, the cell pellets were resuspended in 2-3 mL of the lysis buffer (50 mM HEPES pH 8.0, 500 mM NaCl) per g of cells. The resuspended cells were lysed using a digital sonicator and clarified by centrifugation (15,000 x *g* for 30 min). The clarified lysate was supplemented with imidazole (final concentration of 30 mM) and then applied to a nickel HisTrap column (Cytiva) pre-equilibrated with 10 column volumes (CVs) of the wash buffer (50 mM HEPES pH 8.0, 500 mM NaCl, 30 mM imidazole) at a rate of 4 mL/min. The column was washed with 10 CVs of the wash buffer followed by elution of bound proteins using elution buffer (50 mM HEPES pH 8, 500 mM NaCl, 250 mM imidazole). The elution fractions were analyzed by SDS-PAGE and the fractions containing hSARM1^{TIR} were pooled, supplemented with TEV protease and dialysed into gel-filtration buffer (10 mM HEPES pH 7.5, 150 mM NaCl) for 16-20 h. After dialysis, cleaved hSARM1^{TIR} was reloaded onto the HisTrap column to remove the TEV protease, His_6-tag and contaminants. After the second IMAC step, hSARM1^{TIR} was further purified on a S75 HiLoad 26/600 column pre-equilibrated with gel-filtration buffer. The peak fractions were analyzed by SDS-PAGE, and the fractions containing hSARM1^{TIR} were pooled and concentrated to a final concentration of approximately 4-6 mg/mL, flash-frozen as 10 μL aliquots in liquid nitrogen, and stored at −80°C.

Purification of hSARM1

hSARM1 was expressed as described in the experimental model and subject details section. Cell pellets from 900 mL expressions of SARM1 were resuspended in 20-30 mL of lysis buffer (50 mM HEPES buffer (pH 8.0), 400 mM NaCl, 5% (v/v) glycerol, 0.5 mM TCEP [tris(2-carboxyethyl)phosphine]), lysed using a digital sonicator, and clarified by centrifugation (2 x cycles of 15,000 x *g* for 20 min). The clarified lysate was applied to a nickel HisTrap column pre-equilibrated with 10 CVs of the lysis buffer at a rate of 1 mL/min. The column was washed with 10-20 CVs of lysis buffer supplemented with 20 mM imidazole, followed by elution of bound proteins using elution buffer (50 mM HEPES buffer (pH 8.0), 400 mM NaCl, 250 mM imidazole, 5% (v/v) glycerol, 0.5 mM TCEP). The elution fractions were analyzed by SDS-PAGE and the fractions containing hSARM1 were pooled and further purified on a S200 HiLoad 26/600 column pre-equilibrated with gel-filtration buffer (25 mM HEPES pH 7.4, 150 mM NaCl, 0.1 mM TCEP). The peak fractions were analyzed by SDS-PAGE, and the fractions containing hSARM1 were pooled and concentrated to a final concentration of 5-10 mg/mL and stored at −80°C. For cryo-EM, the IMAC elution fractions were pooled, supplemented with TEV protease, and dialysed into gel-filtration buffer overnight at 4°C. Cleaved hSARM1 was reloaded onto the HisTrap column to remove the TEV protease, His_6-tag and contaminants. After the second IMAC step, hSARM1 was further purified on a S200 HiLoad 26/600 column, concentrated and stored as described above.

^{1}H NMR NADase assays

NMR samples were prepared in 175 μL HBS buffer (10 mM HEPES, 150 mM NaCl, pH 7.5), 20 μL D_2O, and 5 μL DMSO-d6, resulting in a total volume of 200 mL. Each sample was subsequently transferred to a 3 mm Bruker NMR tube rated for 600 MHz data acquisition. All ^{1}H NMR spectra were acquired with a Bruker Avance 600 MHz NMR spectrometer equipped with ^{1}H/^{13}C/^{15}N triple resonance cryoprobe at 298 K. To suppress resonance from H_2O, a water suppression pulse program (P3919GP) using a 3-9-19 pulse sequence with gradients (Piotto et al., 1992; Sklenar et al., 1993) was implemented to acquire spectra with an acquisition delay of 2 s and 32 scans per sample. For each reaction, spectra were recorded at 10 min, 2 h, 4 h, 8 h, 16 h, 40 h, and 64 h time-points, depending on instrument availability. All spectra were processed by TopSpin (Bruker) and Mnova 11 (Mestrelab Research). The amount of NAD^+ consumption was calculated based on the integration of non-overlapping resonance peaks, which vary depending on sample composition, from NAD^+ and NAM, respectively. Likewise, the amount of base exchange was calculated based on those from the base and the base-exchange product, respectively. The detection limit (signal-to-noise ratio > 2) was estimated to be 10 μM.

Production and purification of base-exchange products

Production reactions for **1AD**, **2AD**, and **3AD** were performed using conditions similar to the ^{1}H NMR NADase assays. A solvent volume of 10 mL or 15 mL was used for each reaction, which consists of HBS buffer (50 mM HEPES, 150 mM NaCl, pH 7.5) with 2% (v/v) DMSO. For **1AD** production, 5 mM of His_6-tagged hSARM1^{TIR}, 1 mM **1**, and 1 mM NAD^+ were added to the mixture. For **2AD** production, 0.5 mM of His_6-tagged hSARM1, 1 mM NMN, 10 mM **2**, and 10 mM NAD^+ were added to the mixture. For **3AD** production, 5 mM His_6-tagged hSARM1^{TIR}, 15 mM **3**, and 15 mM NAD^+ were added to the mixture. All reactions were performed at room temperature and monitored intermittently by ^{1}H NMR. To stop the reaction, the His_6 tagged protein was removed by incubating the mixture with 200 mL of HisPur Ni-NTA resin for 30-60 min. The resin was subsequently removed by centrifugation at 500 x *g* for 1 min and the supernatant was subjected to HPLC-based separation to purify the base-exchange products. A Shimadzu Prominence HPLC equipped with a Synergi 4 μm Hydro-RP 80 Å column was used for separation. The mobile phase consists of phase A (0.05% (v/v) formic acid in water) and phase B (0.05% (v/v) formic acid in methanol). Different gradients, flow rates, and run times were applied depending on prior optimization with individual reaction mixtures. Product peaks were confirmed by comparison with individual chromatograms of NMN, NAD^+, NAM, ADPR, and the corresponding base. Fractions corresponding to the product peaks were collected, concentrated, and lyophilized and stored at −20°C.

Characterization of base-exchange products

1AD. ^{1}H-NMR (600 MHz, D_2O): δ 9.70 p.p.m (s, 1H), 8.55 (d, *J* = 6.7 Hz, 1H), 8.39 (d, *J* = 7.4 Hz, 1H), 8.21 (m, 3H), 7.85 (s, 1H), 7.42 (t, *J* = 7.8 Hz, 1H), 6.15 (d, *J* = 4.8 Hz, 1H), 5.76 (d, *J* = 5.8 Hz, 1H), 4.54 (m, 2H), 4.48 (m, 2H), 4.39 (m, 2H), 4.29 (d, *J* = 11.5 Hz, 2H), 4.24 (d, *J* = 11.8 Hz, 1H), 4.16 (d, *J* = 11.6 Hz, 1H); ^{13}C-NMR (150 MHz, D_2O): δ 167.96, 152.29, 149.35, 147.96, 145.93, 140.34, 139.43, 132.12, 131.66, 131.19, 130.25, 127.42, 117.42, 99.50, 96.21, 86.82, 86.25, 83.90, 77.29, 74.23, 70.24, 69.94, 65.48, 64.79; HRMS (m/z): $[M+H]^+$ calcd for $C_{24}H_{27}IN_6O_{13}P_2$, 797.0229; found, 797.0205. Purity > 95% (^{1}H-NMR).

2AD. ^{1}H-NMR (600 MHz, D_2O): δ 9.47 p.p.m (s, 1H), 8.86 (d, *J* = 6.4 Hz, 1H), 8.39 (s, 1H), 8.21 (s, 1H), 8.03 (d, *J* = 6.7 Hz, 1H), 7.70 (d, *J* = 7.9 Hz, 1H), 6.71 (d, *J* = 7.1 Hz, 1H), 6.05 (t, *J* = 4.6 Hz, 1H), 5.95 (t, *J* = 7.3 Hz, 1H), 4.60 (t, *J* = 5.3 Hz, 1H), 4.53 – 4.45 (m, 2H), 4.44 – 4.38 (m, 2H), 4.35 – 4.28 (m, 2H), 4.25 – 4.18 (m, 2H), 4.18 – 4.13 (m, 1H); ^{13}C-NMR (150 MHz, D_2O): δ 161.24, 150.49, 149.76, 148.18, 146.16, 143.39, 141.83, 141.25, 137.48, 125.01, 121.80, 118.09, 104.37, 99.55, 87.54, 86.81, 84.22, 77.27, 74.55, 70.84, 70.34, 65.29, 65.18; HRMS (m/z): $[M+H]^+$ calcd for $C_{23}H_{27}N_7O_{14}P_2$, 688.1164; found, 688.1138. Purity > 95% (^{1}H-NMR).

3AD. ^{1}H-NMR (600 MHz, D_2O): δ 9.38 p.p.m (s, 1H), 8.23 – 8.17 (m, 2H), 7.89 (s, 1H), 7.76 (d, *J* = 7.1 Hz, 1H), 7.52 (t, *J* = 8.0 Hz, 1H), 6.88 (d, *J* = 7.8 Hz, 1H), 6.72 (d, *J* = 8.1 Hz, 1H), 5.90 (d, *J* = 5.8 Hz, 1H), 5.83 (d, *J* = 5.5 Hz, 1H), 4.55 (d, *J* = 5.6 Hz, 1H), 4.51 – 4.44 (m, 2H), 4.40 (m, 3H), 4.34 – 4.31 (m, 1H), 4.28 – 4.20 (m, 2H), 4.19 – 4.13 (m, 1H); ^{13}C-NMR (150 MHz, D_2O): δ 151.66, 148.95, 148.15, 141.09, 140.69, 139.37, 138.75, 137.58, 128.16, 125.45, 117.64, 115.20, 114.20, 113.30, 99.36, 86.99, 86.31, 84.16, 76.88, 74.45, 70.65, 70.40, 65.45, 65.34; HRMS (m/z): $[M+H]^+$ calcd for $C_{24}H_{29}N_7O_{13}P_2$, 686.1317; found, 686.1346. Purity ~80% (^{1}H-NMR).

Enzyme kinetics

The kinetics reaction was carried out in a 384-well plate format with a final volume of 20 μl in assay buffer (HEPES pH 7.4, 0.03% BSA, 10 mM $MgCl_2$, 10 mM KCl) using 2.5 nM purified hSARM1. To test the activation effect of NMN (Figure 1E), NAD^+ at 0, 0.5, 1, 2, 5, 10, 20, 50, 100, 200, 500 μM initial concentration was added after a pre-incubation time of 120 min with 0, 25, 300 μM NMN. To test the inhibition effect of **1** (Figure 1E), NAD^+ at 0, 0.5, 1, 2, 5, 10, 20, 50, 100, 200 and 500 μM initial concentration was added after a pre-incubation time of 120 min with 25 μM NMN and different concentrations of **1** (0, 0.05, 0.15, 0.5, 1.5 μM initial concentration). Incubation was executed at room temperature and stopped upon addition of 40 μl of 7.5% trichloroacetic acid (TCA) in acetonitrile (ACN) after 15 min for the NMN set and 60 min for the **1** set. Samples were centrifuged (10 min, 4350 rpm, RT) and subjected to online-SPE/MS analysis using an Agilent RapidFire 300 (Agilent Technologies, Santa Clara, CA) coupled to a API400 triple quadrupole mass spectrometer (AB Sciex, Framingham, MA). Analytes were desalted on a graphite SPE cartridge (Agilent) using a cycle time of each 3000 ms for load and elute. The mobile phase consisted of water cont. 5 mM ammonium acetate for pump 1 and water/acetonitrile (50/50 v/v) cont. 5 mM ammonium acetate for pump 2 and 3. Substrate and reaction products ADPR and **1AD** were detected in positive electrospray ionisation (ESI) mode by selected reaction monitoring (SRM) of the m/z transitions 560.0/136.1 (ADPR), 797.0/136.2 (**1AD**) and 664.1/136.1 (NAD^+). Concentrations of ADPR and **1AD** were quantified by respective peak areas. All data with 0.5 and 1 μM NAD^+ of the NMN set and with 0.5, 1, 2 and 5 μM NAD^+ of the **1** set were not used for fitting kinetics properties (k_{cat} and K_M) as more than 20% of either initial NAD^+ or initial **1** had been consumed. Fitting to Michaelis-Menten equation was performed by Prism 9.0.0.

NADase inhibition assay

The enzymatic assay was performed in a 384-well polypropylene plate in Dulbecco's PBS buffer in a final assay volume of 20 mL. SAM-TIR lysate, prepared as previously described (Hughes et al., 2021) with a final concentration of 5 μg/mL, was pre-incubated with the respective compound at 1% (v/v) DMSO final assay concentration over 2 h at room temperature. The reaction was initiated by addition of 5 μM final assay concentration of NAD^+ as substrate. After a 2 h incubation at room temperature, the reaction was terminated with 40 mL of stop solution of 7.5% (v/v) trichloroactetic acid in acetonitrile. The NAD^+ and ADPR concentrations were analyzed by online SPE-MS/MS using a RapidFire 300 (Agilent Technologies, Santa Clara, CA), coupled to an API4000 triple quadrupole mass spectrometer (AB Sciex, Framingham, MA).

Analytical size-exclusion chromatography

For analysis of complex size, samples of $hSARM^{28-724}$ were incubated at 1 mg/mL in aSEC running buffer (20 mM HEPES pH 7.5, 150 mM NaCl, 1 mM TCEP) with ligands (**1AD**, **2AD**, NMN, and NAD^+) for 2 h at room temperature. Ligands were used at 0.5 mM, except NAD^+ (2 mM). After incubation, 25 μL of each sample was loaded onto a BioSep 3000 column (Phenomenex) using an Akta Pure device (Cytiva) at 1 mL/min. Analysis of chromatograms and image preparation was performed in Unicorn 7 software (Cytiva).

Crystallization and crystal structure determination

The $hSARM1^{TIR}$ crystals were produced using the hanging drop vapor diffusion method, as described previously (Horsefield et al., 2019). Optimal crystals were obtained via microseeding using 1 μL protein (at a concentration of 3-5 mg/mL in 10 mM HEPES pH 7.5 and 150 mM NaCl) and 1 μL of well solution consisting of 0.1 M Bis-Tris propane pH 7.0, 0.2 M potassium thiocyanate, and 10% (w/v) PEG3350. Consistency of crystal size and quality was greatly improved by microseeding. Compounds **1**, **2** and **3** (final concentration of 10 mM) were soaked into $hSARM1^{TIR}$ crystals in the presence of NAD^+ (final concentration of 10 mM) for 24-48 h. AraF-NAD^+ was soaked into $hSARM1^{TIR}$ crystals (final concentration 5 mM) for 48 h. The crystals were cryoprotected in 20% (v/v) glycerol and

flash-cooled at 100 K. X-ray diffraction data were collected from single crystals on the MX2 beamline at the Australian Synchrotron, using a wavelength of 0.9537 Å. The data-sets were processed using XDS (Kabsch, 2010) and scaled using Aimless in the CCP4 suite (Evans and Murshudov, 2013). The structures were solved by molecular replacement using Phaser (McCoy, 2007) and the hSARM1^{TIR}:glycerol complex (PDB: 6O0R) (Horsefield et al., 2019) as the template. The models was refined using Phenix (Afonine et al., 2012), and structure validation was performed using MolProbity (Chen et al., 2010). The final structures have been deposited in the PDB. Data processing and refinement statistics are provided in Table S1. For the hSARM1^{TIR}:araF-ADPR complex only the ribose that was attached to NAM and the diphosphate group were modeled, because we did not observe electron density for the adenosine moiety and the leaving NAM group.

Cryo-EM sample preparation and data collection

hSARM1: Prior to grid set-up, the protein (0.6 mg/mL) was incubated in gel-filtration buffer (25 mM HEPES pH 7.4, 150 mM NaCl, 0.5 mM TCEP) with 0.5 mM NMN and 0.5 mM **1AD** for 2 h at room temperature. For hSARM1 incubated with 0.5 mM NMN and 2.0 mM NAD^+, the same procedure was followed. For hSARM1$^{28-724}$ incubated with NMN alone, the protein concentration was at 0.3 mg/mL and 0.5 mM NMN was used.

For grid preparation, Quantifoil (Au 300 R1.2/1.3) grids were glow-discharged at 35 mA for 60 s in a GloQube (Quorum Tech). 3 μL of each incubation sample was then applied to the grids, a 3 s blot time was used, and the grids were plunge-frozen in liquid ethane using a Mark IV Vitrobot (Thermo Fisher Scientific, Waltham, MA, USA).

The datasets were collected on a Titan Krios microscope (Thermo Fisher Scientific, Waltham, MA, USA) operated at an accelerating voltage of 300 kV in nanoprobe EFTEM mode, with a 50 μm C2 aperture at an indicated magnification of 81,000x. Movies were collected on a Gatan K3 direct electron detector positioned after a Gatan Quantum energy filter (Gatan, Pleasanton, CA, USA), operated in a zero-energy-loss mode. A slit width of 20 eV was used to acquire dose-fractionated images.

Movies were recorded as compressed TIFFs in super-resolution mode corresponding to a sampling interval of 1.09 Å/pixel (super-resolution 0.543 Å/pix) with an exposure time of 3 s (SARM1:NMN:**1AD** and SARM1:NMN:NAD^+) or 5 s (SARM1:NMN). The total exposure corresponded to 40.9 e-/Å^2 (SARM1:NMN:**1AD**), 45 e-/Å^2 (SARM1:NMN), 42 e-/Å^2 (SARM1:NMN:NAD^+), with the exposure rate of 16 e-/pixel/s (SARM1:NMN:**1AD** and SARM1:NMN:NAD^+) or 9 e-/pixel/s (SARM1:NMN). Images were recorded at −0.5 to −3.0 μm defocus.

hSARM1^{TIR}: Prior to grid set-up, the protein was incubated with 2 mM **1AD** for 1 h at room temperature. For grid preparation, Quantifoil (Au 400 R.2/2) grids were glow-discharged for 60 s in a Diener Femto Plasma Cleaner (Diener Plasma Surface Technology, Ebhausen, Germany). 2 μL of the incubated sample was applied to the grids, a 5 s blot time was used, and the grids were plunge-frozen in liquid ethane using a Mark IV Vitrobot (Thermo Fisher Scientific, Waltham, MA, USA). The datasets were collected on a CRYO ARMTM 300 microscope (JEOL Ltd, Akishima, Tokyo, Japan) operated at an accelerating voltage of 300 kV, at an indicated magnification of 50,000x using an in-column omega energy filter in zero-energy-loss mode with a slit width of 20 eV. Dose-fractionated movies (50 frames) were collected in electron counting mode on a Gatan K3 direct electron detector (Gatan, Pleasanton, CA, USA) using the JEOL Automated Data Acquisition System (JADAS). The calibrated pixel size at 50,000x magnification was 0.96 Å/pixel and the total exposure time was 5 s. The electron dose was 12 e-/pixel/s. Movies were recorded with a defocus range of −0.5 to −2.5 μm.

Cryo-EM data processing

For hSARM1 incubated with NMN and **1AD**, a single dataset containing a total of 8,895 movies were collected and motion correction was performed using RELION 3.1 (Scheres, 2012) Motion Correction. Non-dose weighted micrographs were used for CTF estimation using GCTF (Zhang, 2016). Initial 2D classes were generated from 1645 manually picked particles in RELION 3.1 and were used for template-based picking. 6,108,705 particles were extracted from 8809 CTF-corrected micrographs with a box size of 300 pixels using RELION 3.1. All further processing was performed in CryoSPARC 3.1 (Punjani et al., 2017) (Structura Biotechnology Inc). Following 2D classification, particles were divided for further processing into three groups representing ARM-SAM:NMN (1) and TIR:**1AD** (2) and SAM-TIR:**1AD** (3).

1. For ARM-SAM:NMN, 320,097 particles from the 2D classification were used for ab-initio reconstruction using 2 classes. Heterogeneous refinement was performed using 3 classes. Homogeneous refinement, with C8 symmetry, was performed on the best class (123,256 particles), followed by a final non-uniform refinement (Punjani et al., 2020). The final reconstruction was sharpened using a B-factor of −148.2 Å^2.
2. For TIR:**1AD**, 1,826,067 particles from the 2D classification were used for ab-initio reconstruction using 2 classes. Heterogeneous refinement was performed using 5 classes. 1,066,814 particles from 3 of the classes were subjected to non-uniform refinement. A mask was generated that corresponded to 8 TIR protomers and masked local refinement was performed. The final reconstruction was sharpened with a B-factor of −124.1 Å^2.
3. For the SAM-TIR:**1AD** map, particles from two processing sources were used. The first set of 133,331 particles containing both SAM rings and TIR oligomer were identified from 2D classification. Ab-initio reconstruction was performed with 2 classes, followed by heterogeneous refinement with 4 classes. 66,062 particles from 2 of these classes were selected for further processing. The second set of 320,097 particles were derived from the heterogeneous refinement of the SAM-ARM:NMN

data processing pipeline (volumes 1 and 3, Figure S5). These contained the TIR oligomer along with the SAM-ARM domain. Heterogeneous refinement (3 classes) was performed on this set of particles. 41,112 particles from one of these classes were selected for further processing. Homogeneous refinement was performed on the combined set of 106,888 particles, leading to a final reconstruction which was sharpened with a B-factor of 186.4 $Å^2$. All global resolution estimations were based on using the gold standard Fourier Shell Correlation (FSC) value of 0.143 calculated with two independent half maps.

For hSARM1 incubated with NMN, a total of 6834 movies were collected and motion correction was performed using RELION 3.1. Non-dose weighted micrographs were used for CTF estimation using GCTF. Particles were picked using Topaz (Bepler et al., 2019) in RELION 3.1. 642,433 particles were extracted with a 300 pixel box size from 5,277 CTF-corrected micrographs using RELION 3.1. 2D classification was performed in CryoSPARC 3.1.

For hSARM1 incubated with both NMN and NAD^+, a total of 3181 movies were collected and motion correction was performed using patch-based motion correction. Non-dose weighted micrographs were used for CTF estimation using patch-based CTF estimation. Initial particle picking was performed on 3181 micrographs using the Blob picker in CryoSPARC 3.1. 3,236,212 particles were extracted with a box size of 256 pixels, followed by 2D classification. Template-based picking was performed on the same micrographs using 4 selected 2D classes. 2,851,793 particles were extracted with a 256 pixel box size and 2D classification was performed in CryoSPARC3.1.

For $hSARM1^{TIR}$ incubated with **1AD**, a total of 247 movies were imported into CryoSPARC 3.1 and alignment of movie frames was performed using patch-based motion correction. Fitting of the CTF and defocus estimation was performed using patch-based CTF estimation. Initially, 278 particles were manually picked, extracted using a box size of 400 pixels and subjected to 2D classification to generate templates for automatic particle picking. After template-based automatic particle picking, 35,572 particles were extracted using a box size of 450 pixels. Following multiple rounds of 2D classification, 5,011 particles were used for ab-initio reconstruction using 1 class followed by non-uniform refinement.

Model building and refinement of hSARM1 cryo-EM structures

The $hSARM1^{TIR}$:**1AD** crystal structure and ligand-free hSARM1 (PDB: 7LD0) (Figley et al., 2021), with the TIR domain deleted, were initially fitted as rigid bodies into the cryo-EM maps with UCSF Chimera (Pintilie et al., 2010), using a combination of manual fitting and the 'fit in map' tool. Building of additional residues (311-321) was performed using Coot. The models were then subjected to iterative rounds of molecular dynamics flexible fitting (MDFF) using Namdinator (Kidmose et al., 2019). Following MDFF, the models were subjected to additional rounds of model building and refinement using Coot, ISOLDE (Croll, 2018) and phenix.real_space_refine from the PHENIX suite (Afonine et al., 2018). All model validation was performed using the phenix.validation_cryoem tool (Williams et al., 2018). Images were generated using UCSF Chimera (Pintilie et al., 2010) and UCSF ChimeraX (Goddard et al., 2018).

Structural analyses

The structures were analyzed using the programs PyMol (Schrodinger), PISA (Krissinel and Henrick, 2007), Chimera (Pintilie et al., 2010), Arpeggio (Jubb et al., 2017) and DynDom (Hayward et al., 1997).

SARM1-dependent production of 1AD and 3AD in DRG neurons

Primary DRG cultures were prepared as described in the experimental model and subject details section. For SARM1 activation assays, DRG neurons were infected with the lentivirus expressing human NRK1 at two days in-vitro (DIV). For the **1AD** experiments, neurons (at seven DIV) were treated with vehicle or **1** at a final concentration of 10 μM in the medium with or without NRK1 and NR (100 μM). After four h incubation, metabolites were extracted and **1AD** was measured using LC-MS/MS (Sasaki et al., 2016). For the **3AD** experiments, neurons (at seven DIV) were treated with vehicle or **3** at a final concentration of 10 μM in the medium with NR (500 μM). After six h incubation, metabolites were extracted and **3AD** was measured using LC-MS/MS (Sasaki et al., 2016). Samples were resolved in 5 mM ammonium formate and loaded on HILIC HPLC column (Kinetex 2.6 μm HILIC, 150 × 2.1 mm) with mobile buffer (5 mM ammonium formate). Metabolites were eluted by the MeOH gradient (0-2 min 0% MeOH, 2-6 min 30%–50% MeOH, 6-8 min 50%–80% MeOH, 8-10 min 80% MeOH, 10-15 min 80%–0% MeOH, and 15-25 min 0% MeOH). **1AD** and **3AD** was detected with the mass spectrometer (6470 triple quadrupole, Agilent) with positive mode using following parameters; **1AD**: precursor m/z = 797, product m/z = 136.1, fragmentation = 157 V, collision = 65 V, and cell acceleration = 4 V; **3AD**: precursor m/z = 688.1, product m/z = 373.7, fragmentation = 218 V, collision = 29 V, and cell acceleration = 4 V.

Production of 1AD and 2AD in axotomized DRG neurons

Primary DRG cultures were prepared as described in the experimental model and subject details section. Metabolites from axonal lysates were extracted as described previously (Hughes et al., 2021). At DIV6, all axons were severed using a micro-surgical blade to cut around the cluster of neuronal cell bodies, and axons and supernatants were collected and analyzed separately. **1** and **2** were added 2 h before axotomy. Complete axotomy around the cell bodies cluster was confirmed by ensuring that there were no gaps in the mark left by the blade on the surface of the tissue culture plastic. At the end of treatment, tissue culture plates were placed on ice and culture medium replaced with ice-cold saline (0.9% (w/v) NaCl in water, 500 μL per well). For collection of axonal metabolites, cell bodies were removed using a pipette. For collection of intracellular metabolites, saline was removed and replaced with

160 μL ice cold 50% MeOH in water. The axons were incubated for a minimum of 5 min on ice with the 50% MeOH solution and then the solution was transferred to tubes containing 50 μL chloroform on ice, shaken vigorously, and centrifuged at 20,000 x *g* for 15 min at 4°C. The clear aqueous phase (140 μL) was transferred into a microfuge tube and lyophilized under vacuum. Lyophilized samples were stored at 20°C until measurement. On the day of measurement, lyophilized samples were reconstituted with 15 μL of 5 mM ammonium formate (Sigma Millipore) and centrifuged at 15,000 rpm (20,000 x *g*) for 15 min at 4°C. 10 μL of clear supernatant was analyzed by using LC-MS.

For base-exchange product measurement, lyophilized samples were thawed on ice and suspended in 90 μL of water with 5 mM ammonium formate (Sigma Millipore). The homogenized solution was transferred in injection vials and mixed with 10 μL of internal standard (2-chloroadenosine at 2 ng/μL), of which 75 μL was used for analysis by online solid phase extraction coupled with liquid chromatography and tandem mass spectrometry (XLC-MS/MS). Supernatants from DRG neurons were stored frozen in 1.5 mL Eppendorf tubes, thawed on ice and 10 μL were transferred in an injection vial and mixed with 80 μL of water with 5 mM ammonium formate and 10 μL of internal standard (2-chloroadenosine at 2 ng/μL). 75 μL were used for analysis by online solid phase extraction coupled with liquid chromatography and tandem mass spectrometry (XLC-MS/MS). For online solid phase extraction coupled with liquid chromatography and tandem mass spectrometry (XLC-MS/MS), samples were injected into a SPE cartridge (2 mm inside diameter, 1 cm length, packed with C18- HD stationary phase), part of a SPE platform from Spark Holland (Emmen, the Netherlands). Thereafter, the SPE cartridge was directly eluted on an Atlantis T3 column (3 μm, 2.1 x 150 mm; Waters, Milford, MA, USA) with a water/methanol with 5 mM ammonium formate gradient (0% B for 0.5 min, 0 to 40% B in 6 min, 40 to 60% B in 1 min, 60 to 100% B in 1 min, 100% B for 1 min and back to initial conditions), at a flow rate of 0.15 mL/min to the mass spectrometer. Base-exchange products **1AD** and **2AD** and the internal standard 2-chloroadenosine were analyzed on a Quantiva triple quadrupole (Thermo Electron Corporation, San Jose, CA, USA). Positive electrospray was performed on a Thermo IonMax ESI probe. To increase the sensitivity and specificity of the analysis, we worked in multiple reaction monitoring and followed the MS/MS transitions: **1AD** MH+, 792.5-540.1; **2AD** MH+, 686.4-408.0. The spray chamber settings were as follows: heated capillary, 325°C; vaporizer temperature, 40°C; spray voltage, 3500 V; sheath gas, 50 arbitrary units; auxiliary gas 10 arbitrary units. Calibration curves were produced by using **1AD**, **2AD** and 2-chloroadenosine (Sigma Millipore). The amounts of **1AD** and **2AD** in the samples were determined by using inverse linear regression of standard curves. Values are expressed as ng per 100,000 cells for axons.

Axotomy and quantification of axon degeneration for the SARM1 Y687A mutant

Primary DRG cultures were prepared as described in the experimental model and subject details section. Lentivirus preparation, axon injury, and axon degeneration index has been extensively described elsewhere (Gerdts et al., 2013). Tandem P-2A and T-2A sequences were inserted between Sarm1 and Venus.

QUANTIFICATION AND STATISTICAL ANALYSIS

Statistical data for X-ray crystallography and cryo-EM data collection, refinement and validation are provided in Table 1 and S1. These results were derived from AIMLESS (all crystal structures) (Evans and Murshudov, 2013), Phenix (all structures) (Afonine et al., 2018), MolProbity (all structures) (Williams et al., 2018), and CryoSPARC (all cryo-EM structures) (Punjani et al., 2017). The global resolution estimates of the cryo-EM maps are based on the gold standard Fourier Shell Correlation (FSC) value of 0.143 calculated between two independent half-maps (Chen et al., 2013; Rosenthal and Henderson, 2003; Scheres and Chen, 2012). Local resolution calculations of the cryo-EM map were generated in CryoSPARC (Punjani et al., 2017). For quantification of SARM1-dependent production of **1AD** (Figure 1G) statistical analysis was performed by two-way ANOVA with Tukey post hoc test. $F(2, 48) = 111.5$, $p < 2 \times 10\text{-}16$ among treatments and genotypes (n = 12). For quantification of SARM1-dependent production of **3AD** (Figure S1I) statistical analysis was performed by one-way ANOVA with $F(3,38) = 11.7$, $p = 1.4\text{x}10\text{-}5$ for **3AD**. For quantification of **1AD** and **2AD** in axotomised DRG neurons data represents mean ± SEM, n = 3 (Figures 1H and S1H). Axon degeneration experiments (Figure 6B) were repeated three times (n = 3) and results are mean ± standard deviation.